

# Interstellar Dust Grain Alignment

B-G Andersson,<sup>1</sup> A. Lazarian,<sup>2</sup>  
and John E. Vaillancourt<sup>1</sup>

<sup>1</sup>SOFIA Science Center, Universities Space Research Association, NASA Ames Research Center, Moffett Field, California 94035; email: bg@sofia.usra.edu, jvaillancourt@sofia.usra.edu

<sup>2</sup>Department of Astronomy, University of Wisconsin-Madison, Madison, Wisconsin 53706; email: alazarian@facstaff.wisc.edu

Annu. Rev. Astron. Astrophys. 2015. 53:501–39

First published online as a Review in Advance on  
July 2, 2015

The *Annual Review of Astronomy and Astrophysics* is  
online at astro.annualreviews.org

This article's doi:  
10.1146/annurev-astro-082214-122414

Copyright © 2015 by Annual Reviews.  
All rights reserved

## Keywords

ISM: extinction, ISM: magnetic fields, polarization

## Abstract

Interstellar polarization at optical-to-infrared wavelengths is known to arise from asymmetric dust grains aligned with the magnetic field. This effect provides a potentially powerful probe of magnetic field structure and strength if the details of the grain alignment can be reliably understood. Theory and observations have recently converged on a quantitative, predictive description of interstellar grain alignment based on radiative processes. The development of a general, analytical model for this radiative alignment torque (RAT) theory has allowed specific, testable predictions for realistic interstellar conditions. We outline the theoretical and observational arguments in favor of RAT alignment, as well as reasons the “classical” paramagnetic alignment mechanism is unlikely to work, except possibly for the very smallest grains. With further detailed characterization of the RAT mechanism, grain alignment and polarimetry promise to not only better constrain the interstellar magnetic field but also provide new information on the dust characteristics.

## 1. INTRODUCTION

### 1.1. Optical and Infrared Continuum Polarization

Interstellar polarization was discovered at visible wavelengths over 60 years ago (Hall 1949, Hiltner 1949a) and was almost immediately recognized to be the result of the dichroic extinction of starlight by asymmetric dust grains aligned with respect to the magnetic field (Hiltner 1949b). The complementary polarized emission from the dust was predicted by Stein (1966) and first observed in the far-IR (FIR) by Cudlip et al. (1982). Interstellar medium (ISM) polarization by aligned dust grains has now been probed from the diffuse medium in the UV (e.g., Anderson et al. 1996) to heavily obscured sightlines in the near-IR (NIR) (e.g., Clemens et al. 2012), and into dense clouds and heavily embedded sources using FIR emission (e.g., Dotson et al. 2000).

Such observations both show that the ISM is magnetized and provide a means to infer the geometry and strength of the fields (e.g., Davis 1951, Chandrasekhar & Fermi 1953). Magnetic fields can decisively influence the dynamics of the ISM from hot, diffuse gas to star-forming cores (e.g., Crutcher 2004). The magnetic fields likely strongly affect the earliest stages of star formation in molecular clouds (Crutcher et al. 2009) and also influence the high-energy ISM, shock mediation (Draine et al. 1983), and moderation of heat and mass transport (Balbus 1986, Slavin 1989, Fox et al. 2005). Polarization data also allow constraints on the characteristics of interstellar dust, if the relationship between polarization and field characteristics can be reliably determined. In addition, diffuse dust polarization probes the Galactic foreground emission to the polarized cosmic microwave background (CMB) radiation (e.g., Planck Collab. XIX 2015).

Dust-induced polarization provides an observationally economical probe of all phases of the ISM. However, until recently, the detailed mechanisms for the alignment of the dust grains have been poorly constrained. A quantitative understanding of grain alignment promises to greatly enhance the use of polarimetry to characterize interstellar magnetic fields and other environmental parameters, as well as the dust grains themselves. In this review, we discuss the current state of the field and outline key challenges. The reviews by Lazarian (2007) and Lazarian et al. (2015) present complementary perspectives and additionally address grain alignment in circumstellar and interplanetary media.

Comparisons of the level of polarization with the column density of dust (e.g., Serkowski et al. 1975) show that asymmetric dust grains are the cause of the observed optical and IR continuum polarization. As illustrated in **Figure 1a**, in the optical/near-IR (O/NIR), the upper envelope of the polarization is correlated with the extinction and, thus, the amount of dust along the line of sight. The fractional polarization corresponding to this upper envelope,

$$p/A_V \approx 3\% \text{ mag}^{-1}, \quad (1)$$

while approximately a factor of 3–4 less than calculated for perfectly infinite cylinders (Mathis 1979, Kim & Martin 1994), is observationally universal (e.g., Serkowski et al. 1975, Andersson & Potter 2005, Franco et al. 2010) [we use “fractional polarization” for the observed ratio of polarization to extinction and “polarization efficiency” for the intrinsic value per unit column density (see the sidebar, Polarization Reduction Factors)]. The wide distribution of polarizations suggests that not all environments are equal in producing polarization.

The relationship between the polarization and the magnetic field is deduced by comparing the position angles of the O/NIR polarization with those of synchrotron radiation. The polarization of

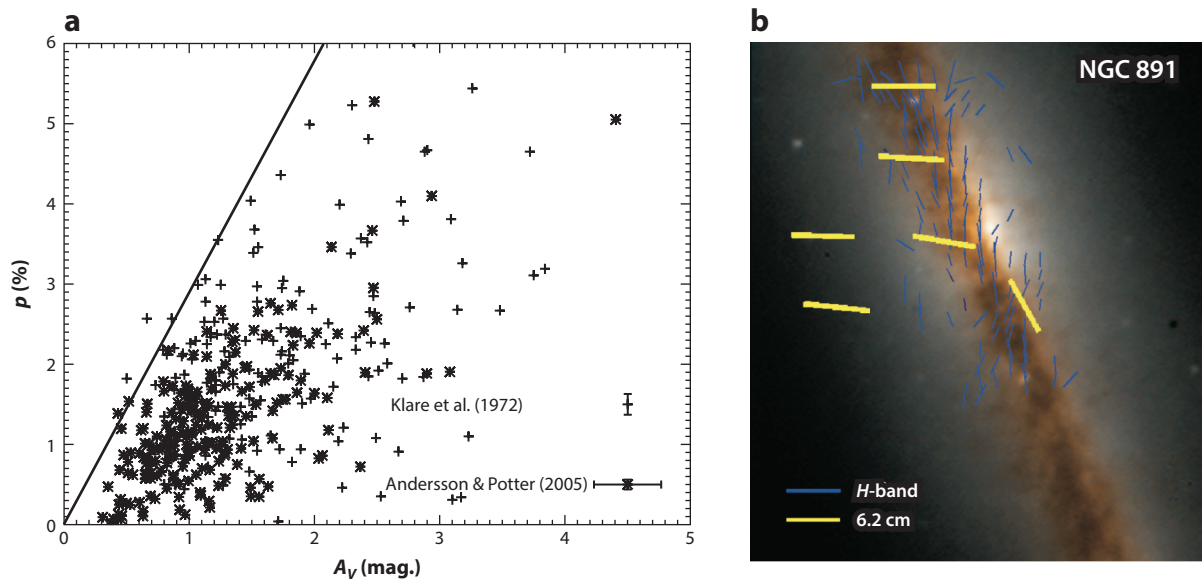


**Figure 1**

(a) The amount of polarization  $p$  as a function of extinction  $A_V$  is bounded by the relation  $p/A_V < 3\% \text{ mag}^{-1}$  (solid line), indicating a correlation between polarization and dust. However, the broad distribution indicates that not all environments produce the same amount of polarization. Reproduced from Andersson (2015) with permission of Springer Science+Business Media. (b) The orientation of the optical/near-IR polarization (blue bars) is systematically orthogonal to that of synchrotron radiation (yellow bars), which itself is known to be orthogonal to the projected magnetic field (courtesy T.J. Jones).

## POLARIZATION REDUCTION FACTORS

Several effects reduce the observed polarization from the ideal estimated from theory. One way to capture this information is the polarization reduction factor (i.e., Lee & Draine 1985),

$$\Phi = RF \cos^2 \gamma,$$

where  $\gamma$  is the inclination of the magnetic field to the line of sight,  $R$  is the Rayleigh reduction factor (a function of the angle between the magnetic field and the precession axis of the grain; Greenberg 1968), and  $F$  is the reduction factor due to a turbulent part of the magnetic field. The measured polarization is then

$$p_{\text{meas}}(\lambda) = \int F \cdot p_{\text{intr}} d\tau = \int F \cdot [\varepsilon(\lambda) R \cos^2 \gamma p_0(\lambda)] d\tau,$$

where  $p_0$  (Equation 4) corresponds to the ideal case, and  $p_{\text{intr}}$  is the polarization per unit column density. The fraction of aligned grains,  $\varepsilon(\lambda)$ , has an explicit wavelength dependence because the alignment may vary with grain size and because the extinction and emission cross sections are functions of grain size. However, there is no such dependence on  $\Phi$ , as it depends only on the magnetic field geometry. Hence, multiwavelength observations provide a natural way to remove the effects of the field geometry, both for O/NIR and FIR observations.

synchrotron radiation is a well-understood phenomenon (Jackson 1975, Burke & Graham-Smith 1997) with a position angle perpendicular to the direction of the magnetic field. Comparing the two types of polarization, one finds that the O/NIR polarization has position angles perpendicular to those of synchrotron radiation (**Figure 1b**) and, therefore, traces the direction of the projected magnetic field. Because the emission cross sections of asymmetric dust grains must be similarly dichroic, one expects, and finds, that the continuum radiation seen in the FIR is similarly polarized, albeit with position angles orthogonal to the O/NIR case.

## 1.2. Interstellar Dust and Grain Size Distributions

Determining the mechanisms responsible for the alignment of the dust grains requires an understanding of the fraction of the total dust grain population that contributes to the polarization in different environments (see Draine 2003). The total grain size distribution can be estimated on the basis of the UV-optical interstellar extinction curve (Mathis et al. 1977, Kim et al. 1994, Clayton et al. 2003) and from emission in the mid-IR (MIR) and FIR together with elemental depletion measurements (Léger & Puget 1984, Draine & Anderson 1985, Désert et al. 1990, Compiègne et al. 2011). Similarly, the distribution of aligned grains can be derived from the wavelength-dependent polarization curve (Mathis 1986, Kim & Martin 1995, Draine & Fraisse 2009). The resulting total grain population is made up of large ( $\sim 0.01$ – $1\ \mu\text{m}$ ) and very small ( $\sim 0.001$ – $0.01\ \mu\text{m}$ ) grains and of polycyclic aromatic hydrocarbon (PAH) macromolecules (e.g., Compiègne et al. 2011). For polarization measurements the large “classical” grains are the most relevant, because, as we shall see below, grains smaller than  $\sim 0.05\ \mu\text{m}$  are typically not aligned in the ISM (however, see Sections 2.1.3, 3.2, and 3.7 below). The overall number density of the large grains was first modeled, on the basis of such observations, by a power-law size distribution with an exponent of approximately  $-3.5$  and grains in the range of  $0.005$ – $0.25\ \mu\text{m}$  (Mathis et al. 1977). Additional models have extended the upper size limit to larger grains, with an exponential decay of number with increasing size (Kim et al. 1994, Clayton et al. 2003, Draine & Li 2007). The dust is usually assumed to consist of silicates, amorphous carbon, and small graphite particles composed of simple shapes (e.g., spheres, spheroids, or cylinders). In the dark, cold parts of molecular clouds grain aggregates may form (e.g., Ysard et al. 2013) as well as mantles of volatile ice materials (Whittet 2003, Boogert et al. 2015 in this volume).

Interstellar polarization in the UV/O/NIR shows a near-universal wavelength dependence (**Figure 2a**), with a maximum typically in the range of  $\lambda = 0.4$ – $0.7\ \mu\text{m}$  that falls off steeply into both the UV and IR. The spectral shape can be parameterized by the following relation:

$$p(\lambda) = p_{\text{max}} \cdot \exp[-K \ln^2(\lambda_{\text{max}}/\lambda)], \quad (2)$$

where  $p_{\text{max}}$  is the maximum amount of polarization at wavelength  $\lambda_{\text{max}}$ , and  $K$  parameterizes the width of the curve (Serkowski 1973).

The relatively narrow width of the polarization curve indicates that only a limited number of grain sizes contribute to the polarization. Detailed modeling (e.g., Mathis 1986, Kim & Martin 1995) shows that the polarization curve can be reproduced from the total grain size distribution if a larger small-size cutoff ( $\sim 0.04$ – $0.05\ \mu\text{m}$ ) is assumed for the aligned grains (Section 3.2). As shown by Kim & Martin (1995), the value for  $\lambda_{\text{max}}$  is a sensitive probe of this small-size cutoff.

Although the  $K$  parameter was originally assumed to be fixed at  $K = 1.15$  (Serkowski 1973), subsequent work (Codina-Landaberry & Magalhães 1976, Wilking et al. 1980) showed that the best-fit value varied from source to source. Wilking et al. (1982) and Whittet et al. (1992) argued that  $\lambda_{\text{max}}$  and  $K$  are likely linearly correlated. As pointed out by Mathis (1986), such a relationship between the center and width of the polarization curve follows naturally if its shape is due solely

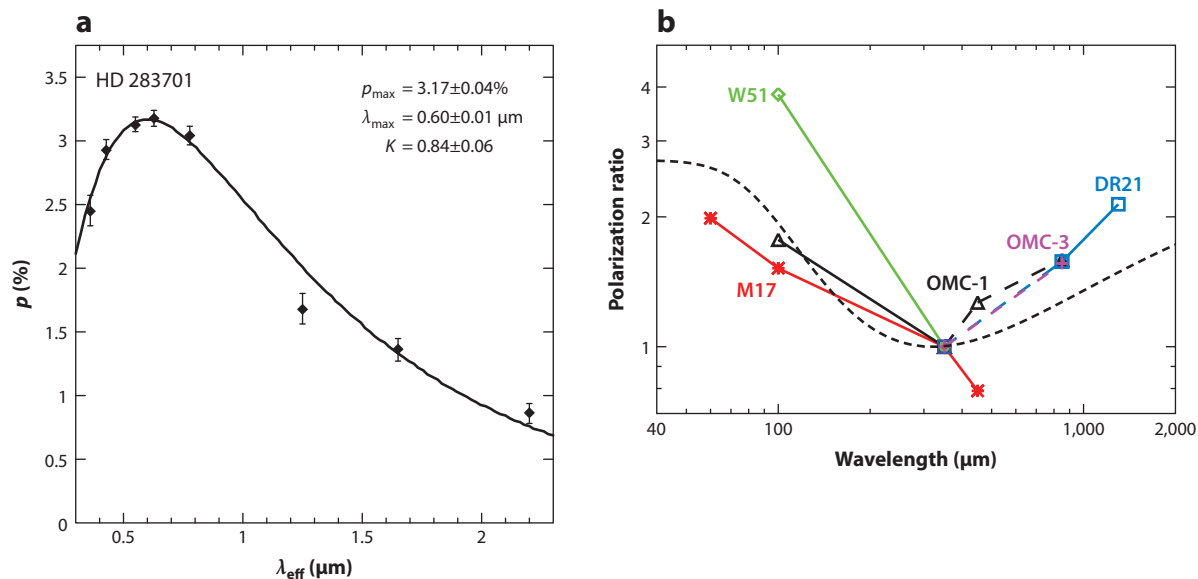


**Figure 2**

(a) The wavelength dependence of interstellar UV/optical/near-IR polarization follows a near-universal relation referred to as the Serkowski relation (Equation 2), illustrated here for the star HD 283701, using data from Whittet et al. (1992). (b) The observed far-IR polarization spectra for a number of molecular clouds (medians for each cloud) show a marked minimum near 350  $\mu\text{m}$  using data from Vaillancourt & Mathews (2012) and Zeng et al. (2013). The dotted line is an illustrative two-temperature dust model. Adapted from Vaillancourt et al. (2008) with permission of the AAS.

to a varying small-grain cutoff in the aligned grain size distribution. Andersson & Potter (2007) showed that a correlation exists between  $\lambda_{\text{max}}$  and  $A_V$  for  $A_V \leq 4$  mag in six different clouds (Section 3.2), indicating that the grain alignment is directly dependent on the visual extinction.

The FIR/millimeter wave polarization spectrum shows a broad minimum around 350  $\mu\text{m}$  for lines of sight in star-forming clouds off of the FIR intensity peak (**Figure 2b**). As shown by Hildebrand et al. (1999), a single population of grains cannot produce this polarization spectrum. At minimum, a two-component dust population is required with either significantly different wavelength-dependent grain emissivities or temperatures (e.g.,  $T_{\text{hot}} \sim 2T_{\text{cold}}$ ; Vaillancourt 2002). Their preferred model, yielding the drop in polarization from 60 to 350  $\mu\text{m}$ , is one in which the components (along the line of sight and within the telescope beam) differ in temperature, and the warmer dust component is better aligned. Vaillancourt et al. (2008) showed that the rise in the polarization spectrum beyond 350  $\mu\text{m}$  can, in such a two-component model, be understood as an effect of different grain emissivities. Hence, grain alignment is seen to vary with environment, which can provide observational constraints to the underlying physics.

### 1.3. Grain Alignment

For significant polarization to be generated by aligned, asymmetric grains, two conditions must be met: (a) The grains must have their angular momentum vectors aligned in space, and (b) the angular momentum vector of the grains must be aligned with a main grain axis, nominally the axis of maximal moment of inertia (a.k.a. internal alignment). Additionally, the processes that randomize the grain orientation must not overcome the processes driving the alignment. Neither

the internal alignment nor the randomization processes are observationally well constrained. However, on theoretical grounds, general agreement exists that the internal alignment is dominated by relaxation through the Barnett effect (Purcell 1979) and nuclear relaxation (Lazarian & Draine 1999b), whereas the randomization—for large grains in neutral gas—is dominated by gas-grain collisions (Draine & Lazarian 1998b).

The first theory for interstellar grain alignment was formulated by Spitzer & Tukey (1949) and relied on ferromagnetic grains, aligned equivalently to the manner in which a compass needle aligns itself with the magnetic field of the Earth. However, for grains with temperatures typical of the diffuse ISM, this ferromagnetic alignment requires a significantly stronger interstellar magnetic field than is typical in the Galaxy (Richtmyer & Teller 1949). Subsequently, three main grain alignment paradigms have been proposed: paramagnetic relaxation, mechanical alignment, and radiative alignment.

Davis & Greenstein (DG) (1951) proposed a relaxation mechanism wherein the dissipation of the magnetization energy aligns the spin axis of the grain with the local field. Several clarifications and modifications to this paradigm were subsequently introduced, including a number of new physical effects: magnetic moments arising from the Barnett effect (Dolginov & Mytrophanov 1976), the alignment of the grain axes with respect to the angular momentum (Purcell 1979), and the description of internal thermal wobbling of grains (Lazarian 1994, Lazarian & Roberge 1997a). Enhancements were also proposed that rely on stronger magnetic susceptibility in the grain, by the inclusion of ferromagnetic subgrains (superparamagnetism; e.g., Jones & Spitzer 1967, Mathis 1986), and on the spin-up of the grains to angular velocities well above those of the thermal energies of the system. The latter enhancements are primarily due to the ejection of newly formed  $\text{H}_2$  molecules from the grain surface (suprathermal rotation; Purcell 1979).

A second general alignment mechanism was proposed by Gold (1952a,b), who noted that, for a systematic flow of gas particles past an elongated dust grain, the grain tends to tumble, aligning the spin axis perpendicular to the flow. To be effective, this requires supersonic relative flows (Lazarian 1997 and references therein). Several processes have been proposed (Section 2.2) to accomplish the relative gas-dust motion, including cloud-cloud collisions (Gold 1952b), the transverse motion of Alfvén waves (Lazarian 1995), and the cyclotron orbital motion of charged particles around the magnetic field (Yan & Lazarian 2003). For stars that exhibit outflows and intensive stellar winds, numerical models (see Netzer & Elitzur 1993) predict a supersonic relative drift of grain and gas that could result in mechanical alignment.

A third alignment paradigm, based on the angular momentum transfer inherent in the scattering of light by a dust grain, was originally introduced by Dolginov & Mytrophanov (1976) and relies on the differences in scattering efficiency for right- and left-hand circularly polarized light off of a grain with some net helicity. For grains made up of a paramagnetic material, having acquired a magnetization through the Barnett effect, the grains are then aligned with the magnetic field through the continuing radiative torques over their Larmor precession period. The detailed dynamics of the grain alignment is complex and generally requires the analysis of phase space trajectories of the system (see the sidebar, ISM Grain Alignment Proceeds Through Nonlinear Dynamics).

Although there are likely specific circumstances in which each of these alignment mechanisms may dominate, we shall argue that a preponderance of theoretical and observational evidence now points to the radiative alignment torque (RAT) mechanism as the best explanation of the observed optical/infrared (O/IR) and FIR/millimeter polarization in the ISM. A number of specific theoretical predictions made by the three paradigms have been experimentally tested over the past decade, placing severe constraints on the viability of paramagnetic and mechanical alignment while supporting RAT alignment. **Table 1** summarizes these tests. We shall focus our discussion on the predictions and results of RAT alignment.

## ISM GRAIN ALIGNMENT PROCEEDS THROUGH NONLINEAR DYNAMICS

The dynamics of radiatively aligned dust grains are nonlinear and sensitively dependent on initial conditions. As a result, analyzing the motion of a dust grain requires a statistical approach in which the dynamical evolution (or trajectory) of the grains is followed in a phase space diagram. The analysis of such nonlinear dynamics is often referred to as Chaos Theory (e.g., Lorenz 1993). Stationary points in such diagrams are referred to as attractor points if they are stable and repeller points if they are unstable. The stable attractor points are states into which the system evolves independent of minor changes in the initial conditions.

## 2. THEORY OF INTERSTELLAR GRAIN ALIGNMENT

The theory of grain alignment is an extensive subject that is impossible to cover in depth within this review. Thus our focus shall mostly be on the RAT mechanism, which, as we shall discuss in Section 3, is supported by recent observations of interstellar dust polarization. More details on paramagnetic and mechanical grain alignment can be found in an earlier review by Lazarian (2003).

### 2.1. Alignment by Paramagnetic Relaxation

The textbook DG mechanism (Davis & Greenstein 1951) is based on the paramagnetic dissipation of energy in a rotating grain and spun up by collisions with the gas. The grains align with the magnetic field, owing to dissipation of the angular momentum components perpendicular to the field, if the relaxation time  $t_{\text{DG}}$  is much shorter than the randomization time through gaseous collisions,  $t_{\text{gas}}$ .

**2.1.1. Historic perspective.** In practice, the DG alignment condition is difficult to satisfy in the diffuse ISM. For grains with  $a = 0.1 \mu\text{m}$ , a magnetic field of  $5 \mu\text{G}$ , and gas temperature

**Table 1** Summary of grain alignment results to date<sup>a</sup>

Observation	Larger grains are better aligned	General alignment only active for $a > 0.045 \mu\text{m}$	H <sub>2</sub> formation enhances alignment	H <sub>2</sub> formation not required for alignment	Alignment seen when $T_{\text{gas}} = T_{\text{dust}}$	Alignment is not correlated with ferromagnetic inclusions	Alignment is lost at $A_V \sim 20 \text{ mag}$	Alignment depends on angle between radiation and magnetic fields	Carbon grains are unaligned
<b>Theory</b>									
Davis-Greenstein	—				—				
Super-paramagnetic	+				—	—			
Suprathermal			+	—					
Mechanical			—				—		—
Radiative alignment torque	+	+	+				+	+	+

<sup>a</sup>Green plus sign (+), observational support of a specific theoretical prediction; red minus sign (—), a contradiction between theory and observations. Gray boxes indicate no prediction or ambiguous results.



and density of 100 K and  $20 \text{ cm}^{-3}$ , respectively, the timescales are  $t_{\text{DG}} \approx 7 \times 10^{13} \text{ s}$  and  $t_{\text{gas}} \approx 3 \times 10^{12} \text{ s}$ . The concepts of superparamagnetic grains (Jones & Spitzer 1967) and suprathermal rotation rates (Purcell 1979) were introduced to overcome this problem (see also Section 2.3.4).

Suprathermal grains rotate fast owing to external regular torques, so-called Purcell torques, arising, for example, from photoelectric emission or the formation of  $\text{H}_2$  on grain surfaces, making them much less sensitive to thermal gas collisions. However, as the direction of the torques changes, a grain may decelerate to low values of angular momentum. At this point, the internal alignment between the angular momentum and the axis of maximal inertia may be lost, which may also result in a crossover event in which the rotational direction of the grain flips with respect to the angular momentum (for details see Spitzer & McGlynn 1979, Lazarian & Draine 1999a). In the absence of random torques the grain after a crossover may reaccelerate, thereby rotating with the same orientation as before the crossover. However, in the presence of gaseous bombardment the angular momentum can be partially randomized. The most critical time for grain randomization during a crossover event is the time just prior to, and after, the grain flip, when the grain rotation is subthermal (Spitzer & McGlynn 1979). The crossover theory was subsequently modified to include thermal wobbling (Lazarian 1994, Lazarian & Roberge 1997a). An improved version of the paramagnetic dissipation theory, incorporating these elements, predicted very encouraging degrees of alignment (Lazarian & Draine 1997).

As discussed by Lazarian & Draine (1999a; cf. Hoang & Lazarian 2008), the internal excitations in a grain with nonzero temperature (e.g., phonons) can couple to the macroscopic motion of the grain, including causing the grain to flip while in a low angular momentum state. For a spin-up mechanism fixed in the grain coordinate system, such as Purcell alignment, the sign of the torque (in space coordinates) changes upon such a flip. The efficiency of the nuclear relaxation mechanism (Lazarian & Draine 1999b) means that this leads to “thermal trapping” of the grains at low angular momenta and, therefore, that the grain does not achieve suprathermal spin rates. This made the paramagnetic alignment of large grains ( $a > 0.1 \text{ }\mu\text{m}$ ) less efficient for a range of grain sizes in which the alignment is seen observationally.

As discussed in Section 2.3.5, the most serious issue with the dominance of the paramagnetic alignment in the ISM is that the RATs are much stronger than the DG torques. Nevertheless, for sufficiently small grains, RAT alignment is less efficient than paramagnetic alignment such that the DG mechanism may be necessary to account for grain alignment (Lazarian & Draine 2000; Hoang et al. 2013, 2014).

**2.1.2. Paramagnetic alignment of small grains.** The efficiency of paramagnetic alignment increases with decreasing grain size, and modeling (e.g., Hoang et al. 2013) shows that a finite degree of small-grain alignment is needed to reproduce observations. Although the analysis of Kim & Martin (1995) suggests that interstellar silicate grains of size  $a > 0.05 \text{ }\mu\text{m}$  are well aligned, in good agreement with RAT theory predictions (Section 3.2), they also noticed features that can be attributed to a residual small-grain alignment ( $a \sim 0.01 \text{ }\mu\text{m}$ ). This is in agreement with the results of Clayton et al. (1992, 1995), who found evidence for residual alignment of small grains based on a UV polarization greater than that predicted by the Serkowski function and longer wavelength measurements. The more recent analysis by Draine & Fraisse (2009) supports these findings and indicates for small grains a degree of alignment of  $\sim 1\%$  with only silicate grains aligned.

Although RAT alignment dominates the large grains, it is unclear whether it can also explain the small-grain alignment. For instance, most of the stars with observed UV polarization excess do not also show evidence of the special conditions required for RATs to align small grains, i.e., aligning photons with  $\lambda < 912 \text{ }\text{\AA}$ . For instance, one would expect to observe excess emission at



60  $\mu\text{m}$  attributable to the additional UV radiation acting upon small grains. In contrast, apart from HD 197770 (Clayton et al. 1995), such excess 60- $\mu\text{m}$  emission is not seen for stars exhibiting UV polarization. The favorable estimates for the alignment of very small grains, discussed below, therefore make the idea of paramagnetic alignment attractive in this case.

Hoang et al. (2014) showed that the enhanced alignment of small grains, required to explain the UV observations, could be achieved through alignment by paramagnetic relaxation under the assumption of an increased magnetic field strength. They derive an upper limit for the required interstellar magnetic field of  $B \sim 10 \mu\text{G}$  for the typical ISM regions in which  $\lambda_{\text{max}} = 0.55 \mu\text{m}$ . To reproduce the UV polarization excess in lines of sight with low  $\lambda_{\text{max}} = 0.51 \mu\text{m}$ , the field must increase to  $B \sim 15 \mu\text{G}$ . These values are somewhat larger than the values obtained through Zeeman measurements (Crutcher et al. 2009) but are within the range of measured magnetic field variations. It is noteworthy that whereas Zeeman measurements and the Davis-Chandrasekhar-Fermi method are only sensitive to the line of sight, or plane of the sky, components of the magnetic field, respectively, small-grain paramagnetic alignment probes the total magnetic field strength.

As the small-grain paramagnetic alignment is predicted to depend on the magnetic field strength, it may, in conjunction with observational parameters such as  $p_{\text{max}}$ ,  $\lambda_{\text{max}}$ , and  $p_{\text{UV}}$ , provide another observational method for constraining the field strength (Hoang et al. 2014). This method would be complementary to other techniques for constraining the interstellar magnetic field, such as the Zeeman effect (e.g., Crutcher et al. 2009), the Davis-Chandrasekhar-Fermi method (e.g., Houde et al. 2009), and atomic alignment (e.g., Yan & Lazarian 2015).

**2.1.3. Resonance relaxation and alignment of polycyclic aromatic hydrocarbons.** Lazarian & Draine (2000) showed that the theory of DG relaxation was incomplete for ultrasmall grains ( $a < 1 \text{ nm}$ ) because it ignores the Barnett magnetization produced within the rotating grain. This magnetization arises from the difference between the energy of an electron spin parallel and antiparallel to the grain rotational axis. This difference is proportional to the angular velocity of the grain and is larger for smaller grains. Thus the rotation-induced spin orientation, which can also be called Barnett magnetization, is marginal compared with that induced by intracrystal magnetic fields of large  $a \sim 0.1 \mu\text{m}$  grains but is dominant for ultrasmall grains. This Barnett magnetization is exactly what is needed to induce a paramagnetic resonance within the body of the rotating grain. This process, termed resonance paramagnetic relaxation, is orders of magnitude more efficient than the DG process for rapidly rotating, ultrasmall grains (Lazarian & Draine 2000). A recent numerical study of the consequences of resonance relaxation was conducted by Hoang et al. (2013).

This relaxation process was applied to the alignment of spinning dust, PAHs with electric dipole moments (Draine & Lazarian 1998a,b). Spinning dust is the most likely candidate to explain the anomalous microwave emission at frequencies of 10–100 GHz, first identified in experiments probing the CMB (cf. Kogut et al. 2011; see Section 3.3).

## 2.2. Mechanical Alignment

Mechanical alignment of grains was pioneered by Gold (1952a,b), who considered the interaction of a stick-like grain with gas flowing relative to the dust. He showed that this process causes grains to align with their angular momenta perpendicular to the differential gas-dust flow. Several authors subsequently explored the process through numerical and analytical studies (Dolginov & Mytrophanov 1976, Lazarian 1994, Roberge et al. 1995).

Originally, Gold (1952b) considered cloud-cloud collisions as the means to produce the required gas-dust flow, with magnetic fields playing no role in the alignment. However, this results

in an alignment direction inconsistent with observations. For gas flows along the magnetic field direction, the predicted polarization also is in conflict with observations. Later, Lazarian (1994, 1995) employed Alfvénic turbulence to drive the gas-dust flow and showed that the alignment induced by this type of flow is in agreement with observations, that is, with polarization parallel to the magnetic field direction. This conclusion was strengthened by studies of grain acceleration by magnetic turbulence (cf. Yan & Lazarian 2002, Hoang et al. 2012).

In the presence of suprathermal rotation, the Gold mechanical alignment method fails, as it was originally formulated for thermally rotating grains. However, Lazarian (1995) introduced two new alignment processes, termed cross-sectional and crossover alignment, that allow grains to align even in the case of fast rotation (cf. Lazarian & Efrimsky 1996, Lazarian et al. 1996). Mechanical cross-sectional and crossover alignment can potentially compete with paramagnetic processes for the alignment of small grains. However, the efficiency of grain acceleration by magnetic turbulence drops for very small grains, making the efficiency of mechanical alignment unclear.

Lazarian & Hoang (2007b) showed that helical grains can also be mechanically aligned by subsonic flows, in a manner analogous to radiative spin-up. However, this mechanism is less efficient than RAT alignment because irregular grains interact with radiation and gas bombardment differently. Radiation interacting with a typical  $0.1\text{-}\mu\text{m}$  grain samples the entire grain volume, meaning that the grain has a fixed helicity. In contrast, the gas interacts only with the different facets of the grain surface exposed to the flow over time, causing the effective helicity to change as the grain rotates. Numerical calculations (T. Hoang, A. Lazarian, and J. Cho, in preparation) confirm the analogy between mechanical and RAT alignment for simple irregular shapes. For more complex shapes, very complicated dependencies arise for the torques. The extent to which the torques, introduced by Lazarian & Hoang (2007b), influence grain dynamics is a challenge for future research.

### 2.3. Radiative Alignment

Radiative grain alignment originates in the differential extinction cross sections for the left- and right-hand circular polarization components of light incident upon an irregular grain. This asymmetry results in torques on the grain, leading to increased angular momentum (i.e., spin-up). For grains composed of paramagnetic material, a net internal magnetization follows via the Barnett effect. In the presence of an external magnetic field the magnetized grain Larmor precesses around the field direction. The continued action of the radiative torques over the precession period aligns the angular momentum of the grain with the magnetic field, yielding the observed alignment of the grain and the magnetic field.

**2.3.1. Historic perspective.** Radiative torques as a possible grain alignment mechanism was first introduced by Dolginov & Mytrophanov (1976) but, for the most part, was subsequently ignored for the next 20 years. The availability of powerful computers allowed Draine & Weingartner (1996) to apply the discrete dipole approximation, embodied in the DDSCAT code (Draine & Flatau 1994), to perform detailed scattering calculations and thereby demonstrate that RATs can dominate other torques acting on interstellar grains. These torques can spin the grains up to suprathermal velocities and also act to align the grains. In the presence of a magnetic field the grain rotational axis precesses about the field while the radiative torques act to align the grain with the field (Draine & Weingartner 1997). This confirmed the prediction by Dolginov & Mytrophanov (1976) that anisotropic radiation itself induces alignment (see also Weingartner & Draine 2003).

Analytical calculations of a model grain by Dolginov & Mytrophanov (1976) suggested possible alignment of the grain long axes both parallel and perpendicular to the magnetic field, depending

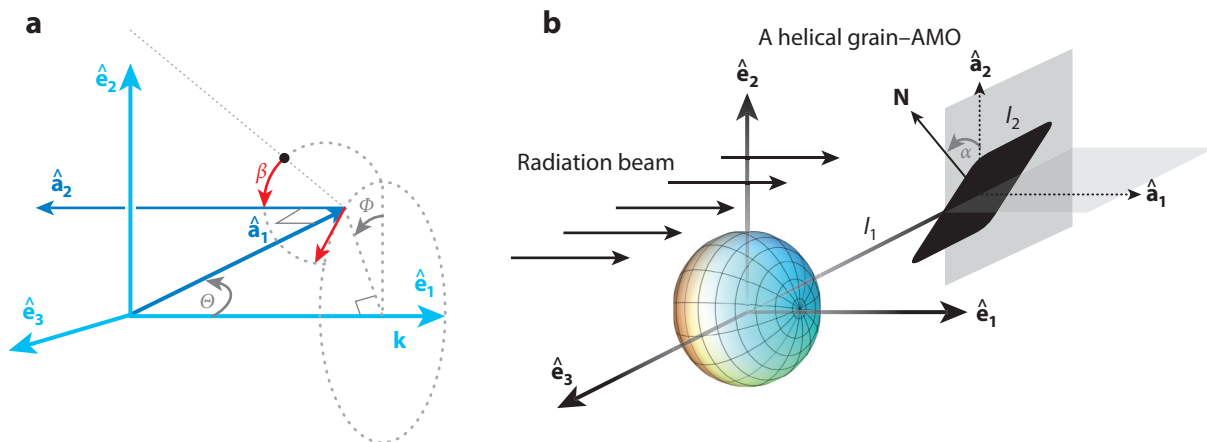


**Figure 3**

(a) The orientation of a grain, described by three principal axes  $\hat{a}_1$ ,  $\hat{a}_2$ , and  $\hat{a}_3$ , in the laboratory coordinate system (scattering reference system with axes  $\hat{e}_1$ ,  $\hat{e}_2$ , and  $\hat{e}_3$ ) is defined by three angles,  $\Theta$ ,  $\beta$ , and  $\Phi$ , in which the direction of the incident photon beam  $\mathbf{k}$  is along  $\hat{e}_1$ . The symmetry axis of the grain,  $\hat{a}_1$ , is at an angle  $\Theta$  with respect to the radiation, and  $\Phi$  is the precession angle of the grain axis about the radiation direction. (b) A model of a helical grain used to analytically compute radiative alignment torques induced by radiation in the same scattering coordinate system, in which  $\Theta = 0$  for simplicity only. A perfectly reflecting oblate spheroid is connected to a weightless mirror of length  $l_2$  by a rod  $l_1$ . The vector normal to the mirror,  $\mathbf{N}$ , lies in the plane  $\hat{a}_1\hat{a}_2$  with angle  $\alpha$  to  $\hat{a}_2$ . Both panels are reproduced from Lazarian & Hoang (2007a). Abbreviation: AMO, analytical model.

on the direction of radiation with respect to the magnetic field. The numerical calculations for three simple, irregular grain shapes in Draine & Weingartner (1997) indicated that the alignment tends to occur with the long axes perpendicular to the magnetic field, for most directions of the impinging radiation, similar to DG alignment. However, this study did not consider grain flipping (see Section 2.1.1). Additionally, because the radiative torques for the three grain shapes were so dissimilar, it was unclear what exactly caused the tendency to produce the correct alignment and whether this tendency was a universal feature of RATs. A subsequent numerical study by Weingartner & Draine (2003) completed the description of the alignment process in Draine & Weingartner (1997), establishing that RATs not only accelerate grains but can also decelerate them and force them into states of slow, near-thermal, rotation rates.

Numerical calculations provide evidence that RATs are important in grain dynamics and yield results in agreement with observations for a limited number of specific cases. However, they do not naturally lend themselves to identifying the underlying physical mechanisms of the grain behavior or its functional dependence on grain and radiation field characteristics. Resolving this problem by a brute force numerical approach, by calculating the interaction between hundreds of grain shapes with radiation of varying wavelength, would be prohibitively difficult.

This problem was resolved by Lazarian & Hoang (2007a), who circumvented the need for detailed knowledge of the grain shape by identifying the helicity of an irregular grain, interacting with the radiation, as the key property for evaluating the effects of RATs. Because neither spherical nor spheroidal prolate/oblate grains have helicity, the Lazarian & Hoang (2007a) model uses an oblate grain with a weightless mirror attached at an angle to its body (**Figure 3b**), a shape that does have helicity. In this analytical model (AMO), changing the angle at which the mirror is attached produces both left-handed and right-handed model grains. It is obviously not possible to describe all the properties of irregular grains with such a simple model. In particular the model does not attempt to represent the entire complex process of light scattering by such a grain (cf.

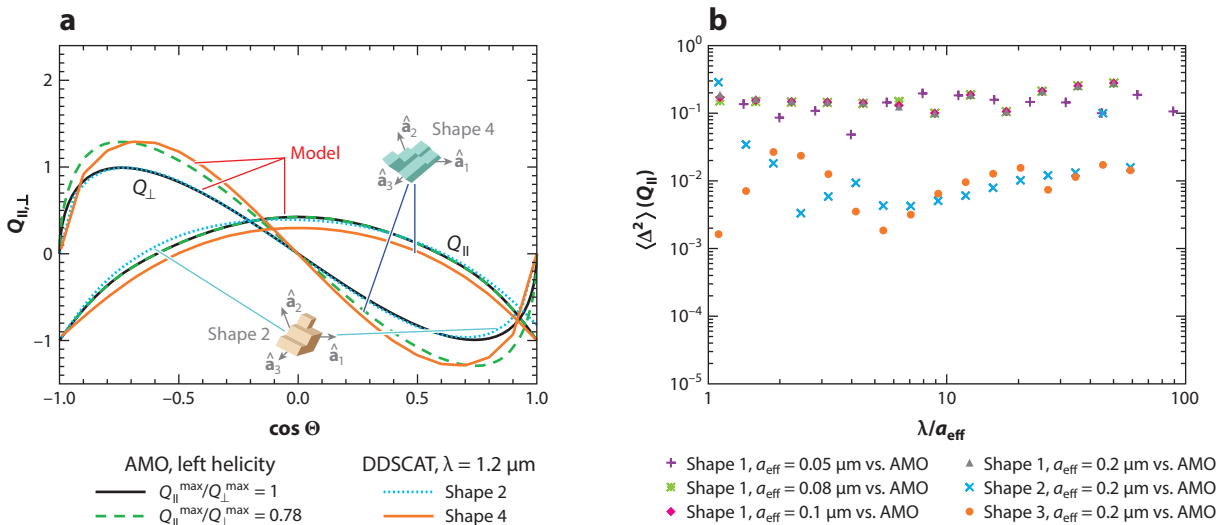


**Figure 4**

(a) Two components of radiative torques, those parallel ( $Q_{\parallel} \parallel \hat{\mathbf{e}}_1$ ) and perpendicular ( $Q_{\perp} \parallel \hat{\mathbf{e}}_2$ ) to the radiation field, are shown as functions of  $\cos \Theta$ . Results computed by DDSCAT for two irregular shapes (shape 2 and 4) are shown for comparison with the analytical model (AMO; adapted from Lazarian & Hoang 2007a with permission). (b) Numerical comparison of the torque  $Q_{\parallel}$  calculated with DDSCAT for irregular grains for different wavelength and the AMO of a helical grain. The quantity  $\langle \Delta^2 \rangle$  is the mean square difference between the two models (see Lazarian & Hoang 2007a for complete definition). Reproduced from Lazarian & Hoang (2007a) with permission.

Dolginov & Mytrophanov 1976). However, the AMO does reproduce the key features found in the numerical DDSCAT calculations (Figure 4b; Section 2.3.3) and provides a number of specific, observationally testable predictions (Section 3).

**2.3.2. Properties of radiative torque alignment.** A key prediction of RAT alignment is that it tends to align the grains with their long axes perpendicular to the magnetic field. This occurs irrespective of the radiation direction, even if the alignment efficiency does depend on this relative radiation-magnetic field direction.

**2.3.2.1. Alignment with the magnetic field.** Within the RAT paradigm, the magnetic field as the axis of alignment follows from the fast precession of the grain rotation axis about the magnetic field. However, this fact alone does not determine whether the angular momentum shall align parallel or perpendicular to the magnetic field. The form of the torques acting on a helical grain suggests that the alignment with angular momentum parallel to the magnetic field is much more likely (Lazarian & Hoang 2007a). In what follows, we illustrate the action of RATs for the case in which the angular momentum axis  $\mathbf{J}$  is perfectly aligned with the maximal inertial moment of the grain,  $\mathbf{a}$ . Although this internal alignment ( $\mathbf{J}$  perpendicular to the long axis) is nearly perfect for suprathermally rotating grains (see the sidebar, Dissipation of Energy; also Purcell 1979, Lazarian & Draine 1997, Lazarian & Efrimsky 1999), the complete theory does consider the general case of partial internal alignment and crossovers with large misalignments (Lazarian & Hoang 2007a, Hoang & Lazarian 2009b).

In the case of perfect alignment with  $\mathbf{J} \parallel \mathbf{a}$  it is sufficient to follow the dynamics of the angular momentum when determining the alignment of the grain axis with the magnetic field. Referring to

## DISSIPATION OF ENERGY

Both the Barnett effect and paramagnetism (the ordering of internal spins in response to an applied, external field) involves a finite response time in the solid, requiring the reordering of spins in response to external forces. If the time variation of the external process (e.g., grain rotation, nutation, etc.) is faster than the response of the material, the imaginary part of the magnetic susceptibility becomes dynamically important, resulting in dissipation of the energy stored in the magnetization into heat (Purcell 1979, Lazarian & Draine 1999b).

**Figure 5**, we denote the torque component parallel to the grain angular momentum as the spin-up torque  $\mathbf{H}$ , and the component perpendicular to  $\mathbf{J}$  and in the plane of the figure as the alignment torque  $\mathbf{F}$ . The alignment is described in terms of only these two torques. Due to the Barnett effect, a spinning paramagnetic grain acquires a magnetic moment, thereby causing the angular momentum  $\mathbf{J}$  to precess around the magnetic field  $\mathbf{B}$  (with the angle  $\xi$  in **Figure 5**). Because the alignment torque  $\mathbf{F}$  is perpendicular to  $\mathbf{J}$ , the fast precession of the grain causes the average value of  $\mathbf{F}$  to approach zero as  $\mathbf{J}$  approaches  $\mathbf{B}$  (i.e., as  $\xi$  decreases). Thus the positions corresponding to  $\mathbf{J}$  parallel with  $\mathbf{B}$  ( $\xi = 0$  and  $\xi = \pi$ ) are stationary points, regardless of the functional forms of the radiative torques. The detailed dynamics of the grain, including whether the stationary points are stable, attractor points, require the full solution of the equations of motion (cf. Draine & Weingartner 1997, Lazarian & Hoang 2007a). Addressing the question of whether the alignment can occur with  $\mathbf{J}$  perpendicular to  $\mathbf{B}$  requires use of the actual AMO expressions for the torque efficiencies with respect to the radiation direction. The narrow range of radiation-to-magnetic

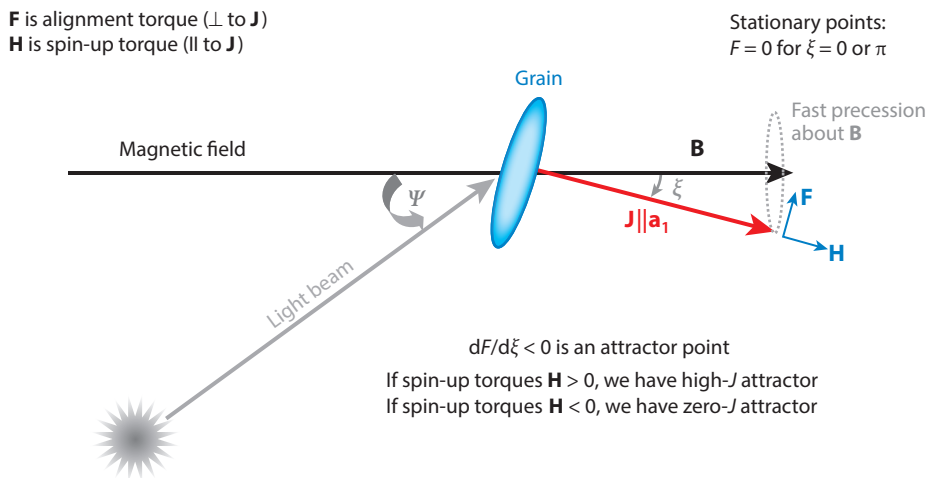


**Figure 5**

A simplified explanation of the grain alignment by radiative torques. The grain, depicted here as an ellipsoid, should, in fact, be irregular in order to generate nonzero radiative torques. The grain has aligned (via internal alignment) with its spin axis  $\mathbf{J}$  parallel to its maximal moment of inertia,  $\mathbf{a}_1$ , and precesses about the magnetic field  $\mathbf{B}$  with angle  $\xi$ . Due to the incident radiation field, at angle  $\Psi$  with respect to  $\mathbf{B}$ , the grain experiences a net torque with components  $\mathbf{H} \parallel \mathbf{J}$  and  $\mathbf{F} \perp \mathbf{H}$ . As shown by Lazarian & Hoang (2007a), the positions  $\mathbf{J}$  parallel (or antiparallel) to  $\mathbf{B}$  correspond to stationary points in which the alignment torque  $\mathbf{F}$ , which changes the angle  $\xi$ , vanishes and the grain becomes aligned with the long axis perpendicular to  $\mathbf{B}$ . Reprinted from Lazarian & Hoang (2011) with permission of the Astronomical Society of the Pacific.

field angles ( $\Psi$ ), for which grains align with their long axes parallel to the magnetic field, occurs in a state of fairly low angular momentum (low- $J$ ; Lazarian & Hoang 2007a), whereas the stationary points above occur at much higher states. In the low angular momentum case, the assumption of perfect  $\mathbf{J} \parallel \mathbf{a}$  alignment does not hold, as thermal fluctuations generate wobbling of  $\mathbf{J}$  about  $\mathbf{a}$ . The resulting range of wobbling angles at the low- $J$  point is much wider than the range of stable angles for which alignment occurs with  $\mathbf{J} \perp \mathbf{B}$  (Hoang & Lazarian 2008). Hence, in the presence of internal excitations and grain wobbling, grains under RAT align with  $\mathbf{J} \parallel \mathbf{B}$ ; that is, they align with their long axes perpendicular to  $\mathbf{B}$ , in agreement with observations.

**2.3.2.2. Helical invariance.** The alignment at high- $J$  attractor points is very efficient and closely aligned with the magnetic field direction. However, if low- $J$  attractor points exist, they too are expected to show a degree of alignment, albeit only on the order of 20–30%. In this respect, the properties of RATs are very different from Purcell torques. The latter are fixed in the grain-body reference frame and, thus, change their direction during crossovers. For a grain acted upon by  $\text{H}_2$  torques, the torque direction can change owing to processes such as grain resurfacing or poisoning of  $\text{H}_2$  formation sites by other species (e.g., Lazarian 1995). Therefore, Purcell torques change with time and accelerate (spin up) the grain rotation at some times but decelerate it (spin down) at other times. The decelerating grain flips when its angular momentum is comparable with the grain thermal angular momentum  $J_{\text{therm}} \sim I k T_{\text{therm}}$ , where  $I$  and  $T_{\text{therm}}$  are the grain moment of inertia and temperature, respectively (Lazarian & Draine 1997). After the flip, the torque fixed in the grain frame changes its direction in space and, instead of decelerating the grain rotation, accelerates it. A grain subject to Purcell torques and in a state of low angular momentum ( $J \sim J_{\text{therm}}$ ) then remains in that state only for the very brief period of a crossover (see Spitzer & McGlynn 1979, Lazarian & Draine 1997). Any stable attractor point must then occur at high- $J$ , that is, in suprathermal rotation.

The situation is different for RATs in which both low- $J$  and high- $J$  states can exist. In the case of RAT, the torques are fixed in space with respect to the radiation direction and not the grain-body reference system. As a result, the torques and phase trajectory map of RAT grain dynamics are symmetric with respect to grain flipping (**Figure 6b**). That is, flipping the grain by  $180^\circ$  in the ambient radiation field does not change the alignment, because grain helicity is invariant under such a flip. Any torque decelerating the grain before a crossover shall also decelerate the grain after the flip, forcing the grain angular momentum to remain near  $J_{\text{therm}}$  and generating low- $J$  attractor points. Thermal fluctuations within the grain material prevent  $J$  from decreasing much below  $J_{\text{therm}}$ , but the grain shall remain in the low- $J$  state owing to the decelerating torque. Another effect of the helical invariance of RATs to grain flips is to make the alignment immune to the effects of thermal trapping.

**2.3.3. Analytical model: main results.** The functional dependence of the torque components in the AMO agrees closely with the torques calculated numerically with DDSCAT for specific irregular grains (Lazarian & Hoang 2007a; **Figure 4b**). The differences between the numerically calculated torques and the analytical predictions are small for all the grain shapes studied (**Figure 4**), implying that much progress in studying the dynamics of RATs can be made using just the AMO without resorting to detailed scattering calculations.

Among the three principal torque components only two contribute to grain alignment. Those components are those parallel ( $\mathbf{Q}_{\parallel} \parallel \hat{\mathbf{e}}_1$  in **Figure 3**) and perpendicular ( $\mathbf{Q}_{\perp} \parallel \hat{\mathbf{e}}_2$  in **Figure 3a**) to the radiation direction. The third component (along  $\hat{\mathbf{e}}_3$  in **Figure 3a**) is also perpendicular to the radiation direction but only induces grain precession, which is subdominant to the Larmor precession of the grain in the magnetic field for most situations. Changing the angle of the mirror



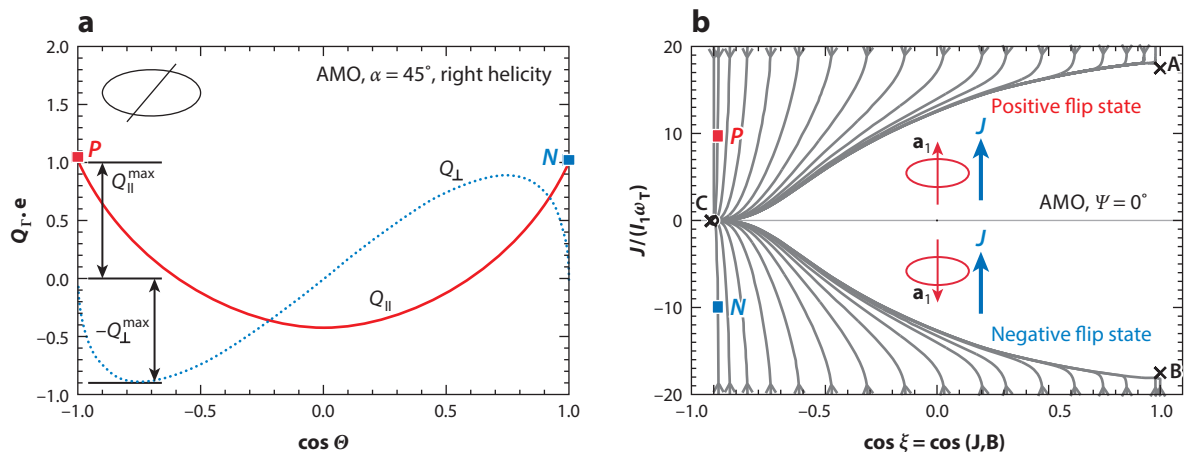


**Figure 6**

(a) Two torque components from the analytical model (AMO) parallel ( $Q_{\parallel}$ ) and perpendicular ( $Q_{\perp}$ ) to the radiation field as a function of the angle  $\Theta$  between the grain spin axis and the direction of radiation (see Section 2.3.3).  $Q_{\parallel}^{\max}$  and  $Q_{\perp}^{\max}$  simply refer to the amplitudes of  $Q_{\parallel}$  and  $Q_{\perp}$ . In this example, the mirror of the AMO is at an angle of  $\alpha = 45^\circ$  with respect to the grain axis (depicted as the line through the ellipse at upper left). Adapted from Lazarian & Hoang (2007a) with permission. (b) A typical phase trajectory map describing the evolution of grain angular momentum ( $J$ ) as a function of the angle  $\xi$  between  $\mathbf{J}$  and the ambient magnetic field, where  $I_1 \omega_T$  is the thermal angular momentum. In this example, repeller points (denoted by “x”) are found at A and B with an attractor point (denoted by “o”) at C, and curves show the path taken by the grain through phase space. Adapted from Hoang & Lazarian (2008) with permission. In the case depicted here in both panels, the grains are subject to radiative alignment torques and rotational gas damping with the external magnetic field  $\mathbf{B}$  parallel to the radiation direction ( $\Psi = 0$ ). The points N and P denote the phase space locations of a  $180^\circ$  flip of the grain, which is equivalent to a flip of the mirror in the AMO. The grain orientation is given by a vector  $\mathbf{a}_1$ , which makes the positive spin state correspond to  $\mathbf{a}_1$  parallel to  $\mathbf{J}$  and the negative spin state antiparallel to  $\mathbf{J}$ . A crossover corresponds to a flipping of  $\mathbf{a}_1$  with respect to  $\mathbf{J}$ . These plots show that such flips do not change the grain dynamics as both the torques and the angular momentum are symmetric in these phase spaces (see Section 2.3.2.2).

with respect to the grain-body changes the amplitude of the torque components,  $Q_{\parallel}(\Theta)$  and  $Q_{\perp}(\Theta)$ . Similarly, grains of different shape exhibit different torque amplitudes. However, the functional form of these torque components with respect to the angle  $\Theta$  between the radiation and grain axis remains approximately the same. Therefore, the amplitudes of these components,  $Q_{\parallel}^{\max}$  and  $Q_{\perp}^{\max}$ —even more simply, their ratio ( $q^{\max} \equiv Q_{\parallel}^{\max}/Q_{\perp}^{\max}$ )—fully determines the RATs of a grain with a given shape in a given radiation field (Lazarian & Hoang 2007a). This enormously simplifies the calculations of radiative torques because, rather than calculating two functions,  $Q_{\parallel}(\Theta)$  and  $Q_{\perp}(\Theta)$ , it is sufficient to calculate just two values,  $Q_{\parallel}^{\max}$  and  $Q_{\perp}^{\max}$ . For instance, the maximum values of the functions  $Q_{\parallel}(\Theta)$  and  $Q_{\perp}(\Theta)$  are achieved for  $\Theta = 0$  and  $\Theta = \pi/4$ , respectively. Thus, the single number  $q^{\max} \equiv Q_{\parallel}^{\max}/Q_{\perp}^{\max} = Q_{\parallel}(0)/Q_{\parallel}(\pi/4)$  characterizes the grain alignment.

As shown in **Figure 4**, the AMO accurately reproduces the DDSCAT behavior of RATs for a given wavelength. To fully reproduce the RAT properties over a range of wavelengths, one must vary  $q^{\max}$ . However, as **Figure 7a** shows,  $q^{\max}$  for irregular grains exhibits regular asymptotic properties as a function of  $\lambda/a$ . Therefore, making  $q^{\max}$  wavelength independent substantially simplifies the modeling.

When grains are aligned at low- $J$  attractor points the RAT-induced alignment is reduced, owing to the thermal wobbling of the grain. However, the alignment is not negligible, as gaseous bombardment can provide the grains with some angular momentum that allows RAT to generate alignment of  $\sim 30\%$ . When both low- $J$  and high- $J$  attractor points coexist, the high- $J$  points are more stable, because such grains are less sensitive to randomization by thermal collisions

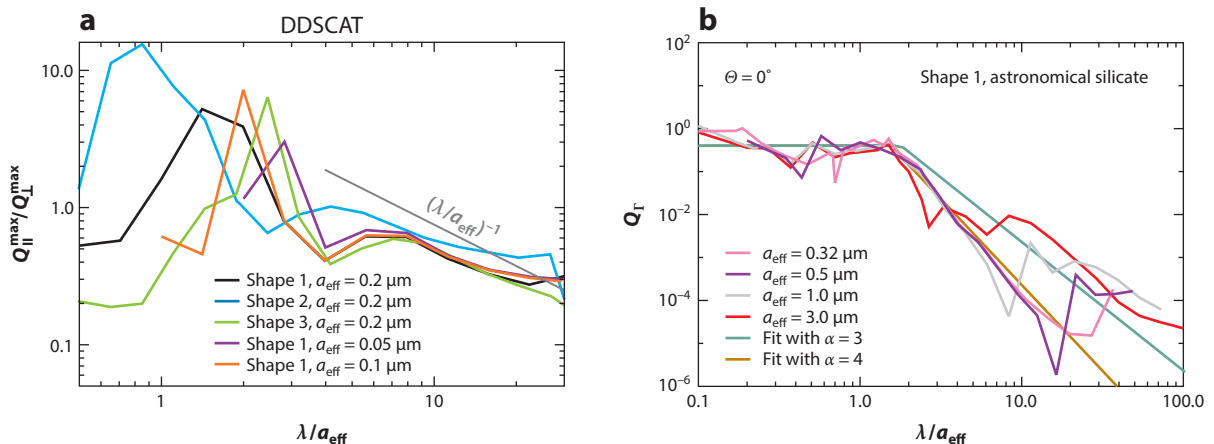


**Figure 7**

(a) Variation of the ratio  $q^{\max} \equiv Q_{\parallel}^{\max}/Q_{\perp}^{\max}$  as a function of illuminating wavelength for various grain shapes and sizes as calculated by DDSCAT. (b) Total torque efficiency  $Q_T$  for grains of different sizes and wavelengths. The most efficient alignment occurs for the larger grains ( $a_{\text{eff}} > \lambda/2$ ). However, the alignment of grains substantially smaller than the radiation wavelength can occur if the radiation is strong enough. Both panels adapted from Lazarian & Hoang (2007a) with permission.

(Hoang & Lazarian 2008). External stochastic driving (e.g., arising from gaseous bombardment) eventually bring the grains to the high- $J$  attractor points, producing perfect alignment. The AMO predicts alignment for cases of both high- $J$  and low- $J$  attractor points, as illustrated by the examples in **Figure 8**.

The amplitude of the total torque efficiency  $Q_T$  varies with grain size and with the wavelength of the illuminating radiation field (**Figure 7b**). As discussed in Section 3.2, this provides a new class of observational predictions. One should also note that the actual physical torque, as opposed to the efficiencies,  $Q_{\parallel,\perp}$  and  $Q_T$ , is proportional to the radiation field intensity (e.g., Draine & Weingartner 1997, Lazarian & Hoang 2007a). As such, the alignment efficiency shall increase with increasing radiation intensity (e.g., Cho & Lazarian 2005, 2007). This means that though the torques decrease rapidly for  $\lambda < 2a$ , they do not, necessarily, become negligible.

**2.3.4. Enhanced radiative alignment.** The aligning torques arising within paramagnetic grains from magnetic dissipation are negligible compared with RATs, but they are appreciable for strongly magnetic grains. Such superparamagnetic, ferromagnetic, and ferrimagnetic grains are expected to be present in the ISM (Goodman & Whittet 1995). For superparamagnetic grains, an attractor point appears in the phase diagram for RAT for cases in which a repeller point was present at high- $J$  for paramagnetic grains (Lazarian & Hoang 2008; **Figure 8a,b**). In the presence of gaseous bombardment, all such grains are expected to reach the high- $J$  attractor point and, thus, a state of perfect alignment. Therefore, the alignment of superparamagnetic grains is enhanced over that of paramagnetic-only grains. However, it is important to note that this is RAT alignment, and not paramagnetic alignment, as the RATs still dominate the grain dynamics.

As discussed above, grains are subject to a number of systematic torques fixed in grain-body coordinates. These so-called pinwheel torques arise from processes such as recoils from  $\text{H}_2$  formation at catalytic surface sites, variations of the accommodation coefficient over a grain surface, photoelectric emission of electrons (all suggested by Purcell 1979), and radiative torques

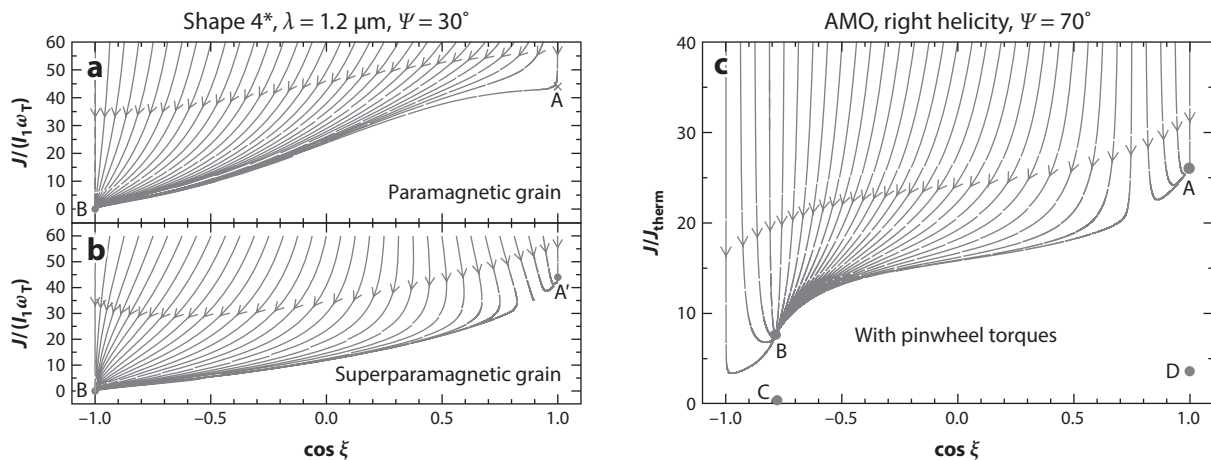


**Figure 8**

Phase trajectories of grains in terms of the angular momentum  $J/(I_1\omega_T)$  ( $= J/J_{\text{therm}}$ ) and the angle  $\xi$  between the grain spin axis and magnetic field. (a) A paramagnetic grain under radiative alignment torque (RAT) has only a low- $J$  attractor point, B, and a repeller point, A. For the same set of parameters a superparamagnetic grain (b) also has a suprathreshold high- $J$  attractor point, A'. The new attractor enhances alignment by providing additional alignment phase space and an attractor point more stable against collisions. The fact that most of the phase trajectories point toward the direction of the low- $J$  attractor illustrates the dominance of the radiative torques for the alignment even in the case of the superparamagnetic grain. Reproduced from Lazarian & Hoang (2008) with permission of the AAS. (c) Grain alignment by RATs in the presence of pinwheel torques. The points C and D correspond to the locations of low- $J$  and high- $J$  attractor points, respectively, in the absence of pinwheel torques. In the case of pinwheel torques, both attractors are lifted to higher- $J$  points (points A and B), thereby enhancing the alignment. Reproduced from Hoang & Lazarian (2009a) with permission of the AAS. Abbreviation: AMO, analytical model.

from thermal emission by the grain (Hoang & Lazarian 2009a). Because they are fixed with respect to the grain-body coordinates, pinwheel torques cannot induce grain alignment themselves but must be followed by some process, such as paramagnetic relaxation (Section 2.1.1; Purcell 1979, Lazarian & Draine 1999b). However, in addition to effecting paramagnetic alignment, the pinwheel torques increase the momentum of the low- $J$  attractor points under RAT alignment, thus creating new attractor points with higher degrees of alignment (Hoang & Lazarian 2009a; **Figure 8b**). Therefore, for sufficiently strong pinwheel torques, one may observe a correlation of the observed polarization with the molecular hydrogen formation rate in the media (Section 3.8; Spitzer & McGlynn 1979, Lazarian 1995, Lazarian & Draine 1997). Because RAT theory predicts perfect alignment of superparamagnetic grains, the addition of pinwheel torques cannot enhance the alignment. Therefore, if enhanced alignment is observed in the presence of pinwheel torques, then not all grains can be superparamagnetic.

**2.3.5. Comparison of radiative and paramagnetic alignment.** DG alignment is still a popular mechanism for dealing with ISM grain alignment in the literature and may still be important in some astrophysical environments. However, in the presence of the much stronger RATs, DG alignment cannot be the dominant mechanism for large  $a > 0.1 \mu\text{m}$  grains. As discussed above, RATs not only introduce grain rotation (Draine & Weingartner 1996), which has been observed in laboratory studies (Abbas et al. 2004), but they also induce grain alignment (Dolginov & Mytrophanov 1976, Draine & Weingartner 1997, Lazarian & Hoang 2007a). Therefore, the effects of DG relaxation on the alignment of large ordinary paramagnetic grains are negligible for a typical

ISM radiation field. Similarly (Section 2.3.4), because of the strength of the RATs, the main effect of regular Purcell torques is not to enhance the DG alignment but to modify the RAT alignment (Hoang & Lazarian 2009a). The same is true for the alignment of grains with strongly magnetic inclusions (Lazarian & Hoang 2008). All in all, theory predicts that unless special requirements for the suppression of RAT alignment are fulfilled, the RAT mechanism shall dominate the alignment, even if paramagnetic relaxation alone could also produce significant alignment (e.g., see Lazarian & Draine 1997). In the following sections we shall show that observations support this assertion.

### 3. OBSERVATIONAL TESTS OF INTERSTELLAR GRAIN ALIGNMENT

The expected polarization from asymmetric grains can be calculated by assuming different opacities to radiation (emitted, absorbed, or scattered) with respect to the principal axes of the grain. For an oblate spheroidal grain with principal axes of size  $x < y = z$ , we can define opacities  $\tau_x < \tau_y = \tau_z$ . For dichroic extinction polarization this yields (e.g., Jones 1989)

$$p_{\text{ext}} = \tanh(\Delta\tau) = \tanh(p_0\tau), \quad (3)$$

where  $\Delta\tau = (\tau_x - \tau_y)/2$  is the differential extinction,  $\tau = (\tau_x + \tau_y)/2$  is the mean opacity, and  $p_0$  is given by

$$p_0 = \frac{\Delta\tau}{\tau} = \frac{\tau_x - \tau_y}{\tau_x + \tau_y} = \frac{C_x - C_y}{C_x + C_y}, \quad (4)$$

where, by convention, we have chosen the order of subtraction such that  $\Delta\tau \leq 0$ . The last equality in the above equation follows from the fact that the opacities are the product of the total column density  $N$  and cross sections  $C_{x,y}(\lambda)$ , such that  $\tau_{x,y}(\lambda) = NC_{x,y}(\lambda)$ . Note we have dropped the wavelength dependence of the above parameters for simplicity only.

For emission the expected polarization becomes (e.g., Hildebrand et al. 2000)

$$p_{\text{emit}} = -\frac{e^{-\tau} \sinh(p_0\tau)}{1 - e^{-\tau} \cosh(p_0\tau)}, \quad (5)$$

where the minus sign denotes the fact that the emission and extinction polarization position angles are orthogonal. In the optically thin case, we find that

$$p_{\text{ext}} = \tau p_0 = -\tau p_{\text{emit}}. \quad (6)$$

#### 3.1. Observed Fractional Polarization

Absent the polarization reduction factors (see the sidebar, Polarization Reduction Factors), the most straightforward observational constraint on grain alignment would be the polarization efficiency,  $p_0$  (Equation 4). In the case of dichroic extinction, the observed fractional polarization follows from Equation 6 such that  $p_0 = p_{\text{ext}}/\tau_V \sim p_{\text{ext}}/A_V$ . For a uniform medium that also contains a fixed grain size distribution and mineralogy, this should correspond to the fraction of the dust grains that are aligned.

Most of the proposed grain alignment mechanisms rely on the presence of radiation with wavelengths less than a critical value. In conjunction with the interstellar extinction curve these wavelengths predict possible opacity break points. Beyond these break points the alignment should become much less efficient, resulting in a drop in the observed fractional polarization. For example, paramagnetic alignment requires that the gas and dust temperatures differ (Jones & Spitzer 1967). If the gas heating is dominated by photoelectric emission from the dust grains (e.g., Wolfire et al. 1995), the opacity for photons capable of initiating such photoelectrons yields a characteristic visual extinction.

A work function of  $\sim 8$  eV (Weingartner & Jordan 2008) corresponds to a wavelength of  $\sim 1550$  Å, which, setting  $\tau(1550 \text{ Å}) = 1$ , yields  $A_V \approx 0.5$  mag. Alignment with suprathermal rotation requires  $\text{H}_2$  formation (Purcell 1979), which implies associated  $\text{H}_2$  photodissociation under statistical equilibrium. Such photodissociation requires the presence of photons with  $\lambda < 1107$  Å, which is equivalent to  $A_V < 0.25$  mag. Finally, RAT alignment requires the presence of radiation with wavelengths less than the grain diameter, which predicts the relation between fractional polarization and extinction if a total grain size distribution is assumed.

A number of authors have used fractional polarization observations to probe for environmental variations in the grain alignment (e.g., Tamura et al. 1987; Jones 1989; Goodman et al. 1992, 1995; Jones et al. 1992; Gerakines et al. 1995; Arce et al. 1998; Whittet et al. 2008; Cashman & Clemens 2014). Most of these studies find a drop in the fractional polarization with extinction following a power law:

$$p/A_V = C \cdot A_V^{-b}, \quad (7)$$

with  $b$  typically close to 0.5. In some cases (e.g., Goodman et al. 1995, Arce et al. 1998), exponents of  $b = 1$  are implied, which indicate the total loss of grain alignment in the inner parts of clouds.

However, a number of observational complications must be considered in interpreting the results. First, because polarization is a vector entity, the amplitude of polarization from independent parts along the line of sight does not necessarily add, depending on the orientation of the local magnetic field, much like crossed polarizers in the lab. Jones (1989) and Jones et al. (1992) modeled polarized radiation through an extended cloud, assuming that the magnetic field consisted of a constant and a random component. When the random component dominates the magnetic field, the expected polarization scales as the square root of the number of turbulent cells traversed, yielding  $b = 0.5$ . For very deep clouds in which the constant magnetic field has a fixed direction, Jones et al. (1992) predicted that the polarization eventually recovers a linear dependence on the column density ( $b \approx 0$ ). However, this change in slope at large  $A_V$  is not seen in the MHD-based simulations conducted by Wiebe & Watson (2001).

Second, the steep rise in ISM opacity toward shorter wavelengths typically requires NIR observations toward high extinction regions. However, the falloff in the Serkowski function (e.g., **Figure 2**) then typically results in polarization of only a few percent even for high column density targets, even when including the enhancements seen beyond the  $K$ -band (Martin et al. 1992). For instance, toward Elias 3–16 in Taurus, with  $A_V = 21.6 \pm 0.4$  mag (Murakawa et al. 2000), the  $K$ -band polarization is only  $p_K = 2.85 \pm 0.05\%$  (Hough et al. 1988). Therefore, high signal-to-noise data at large extinctions require substantial investments of telescope time (see the sidebar, Polarization Uncertainties).

Third, relatively few highly extincted stars have known spectral types and intrinsic colors, causing significant uncertainties in the derived line-of-sight extinction. For most NIR studies the extinctions are calculated via  $JHK$  photometry with an assumed, common, intrinsic stellar

## POLARIZATION UNCERTAINTIES

Because the amplitude of polarization is a positive, definite quantity, calculated from the Stokes parameters,  $p = (q^2 + u^2)^{1/2}$ , the probability distribution of polarization measurements is asymmetric. This results in a positive bias in low signal-to-noise observations. The best estimate of the true polarization  $p'$  is given by the observed value,  $p$ , and its uncertainty  $\sigma_p$  as  $p' = (p^2 - \sigma_p^2)^{1/2}$  (e.g., Vaillancourt 2006, Quinn 2012, Plaszczyński et al. 2014). Because of this bias, polarization measurements with  $S/N \leq 3$  must be used with caution.

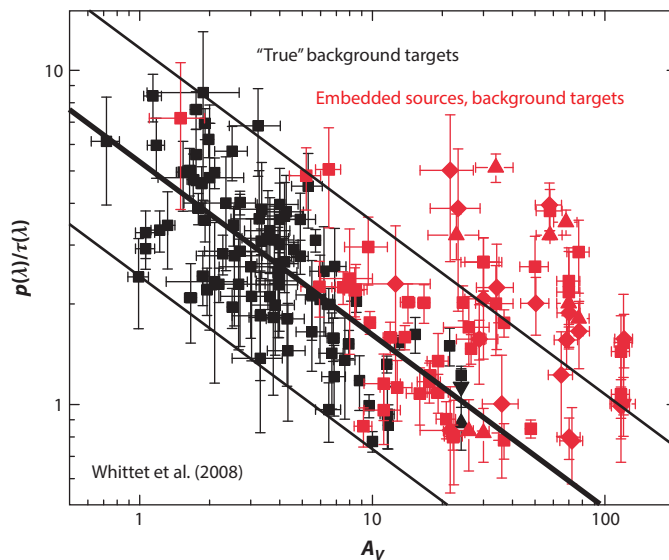


**Figure 9**

The  $K$ -band and ice-feature-based ( $\text{H}_2\text{O}$  and  $\text{CO}$ ) fractional polarization observed in a number of local clouds shows a single power-law decrease over a large range of opacities (*solid lines*). Black symbols indicate background stars, whereas red symbols represent embedded sources. Adapted from Whittet et al. (2008) with permission of the AAS.

color, typically  $(H-K)_0 \approx 0.2$  mag (characteristic of early M stars; cf. Lada et al. 2004) or  $(H-K)_0 \approx 0.02$  mag (characteristic of stars earlier than mid-G). An intrinsic spread in  $(H-K)_0$  of 0.3 mag (A0–M5) implies an uncertainty in  $A_V$  of 4.5 mag (Tokunaga 2000), which can be significant for small samples at moderate extinctions.

**3.1.1. Polarization in medium-opacity clouds.** Although a drop in the fractional polarization with increasing extinction is seen in most medium- to high-opacity clouds, some with  $b > 0.5$  (Goodman et al. 1995, Arce et al. 1998), it is not clear that these signify variations in the grain alignment efficiency. For instance, the break in  $p/A_V$  at  $A_V = 1.3 \pm 0.2$  mag in Taurus reported by Arce et al. (1998) was not seen in subsequent studies (Gerakines et al. 1995, Andersson & Potter 2007, Whittet et al. 2008).

A breakthrough in the use of fractional polarization to study grain alignment was achieved by Whittet et al. (2008), who used a large, high-quality sample of  $K$ -band and ice polarimetry, probing stars behind the Taurus and the Ophiuchus clouds, many with known spectral classes. These data were supplemented by surveys probing LDN 1755 (Goodman et al. 1995) and LDN 1641 (Casali 1995). The sample was separated into true background stars and embedded young stellar objects (YSOs). Whittet et al. find a single power-law exponent, of  $b = (0.52 \pm 0.07)$ , over the full range  $A_V = 0$ –30 mag for the background stars (**Figure 9**). This result is unaffected by the presence or absence of ice mantles on the grains. Many embedded sources also follow this general trend. However, others lie significantly above the trend, indicating enhanced alignment of the grains along these lines of sight. If the embedded stars themselves provide a significant fraction of the illumination of the dust probed, this result strongly supports radiatively driven grain alignment (see Section 3.4).



**3.1.2. Polarization from the cores of starless clouds.** The decline of the Serkowski curve with wavelength into the NIR—as well as the dearth of bright NIR (non-YSO) background sources—makes probing extinction polarization beyond  $A_V \sim 20$  mag very challenging, particularly in clouds without internal sources. Fortunately, at such large opacities dust emission becomes sufficiently bright to measure polarization. Using Equation 6, extinction and emission polarization can be directly compared by scaling the emission polarization with the dust opacity (e.g., Hildebrand 1988). Although the absolute scaling between the two is uncertain due to the grain emissivity and temperature distributions, the relative behavior can be reliably compared. Such studies have recently been carried out for star-less cores by Alves et al. (2014) in cloud 109 of the Pipe nebula, by our group in LDN 183 (B-G Andersson, J.A. Acosta Pulido, J.E. Vaillancourt, M. Charcos Llorens, S.S. Shenoy, in preparation) and by Jones et al. (2015). In all these studies extensive surveys using optical, NIR, and submillimeter data were combined to map the fractional polarization from the cloud surface to  $A_V = 50$ –100 mag. Recent results from the *Planck* mission (Planck Collab. XIX 2015) also indicate a decrease in the observed polarization fraction with increasing column density at  $N_H > 2 \cdot 10^{22} \text{ cm}^{-2}$ . Whole-sky distribution plots of polarization fraction versus column density show a steep drop in the maximal and average relation between  $p$  and  $N_H$  beyond this point, which is consistent with an exponent of  $b \approx 1$ .

For LDN 183, we have assembled equivalent  $H$ -band fractional polarization over  $A_V \approx 0$ –100 mag. The observed  $R$ -band polarimetry was transformed onto an  $H$ -band scale using an average, opacity-dependent Serkowski curve (Andersson & Potter 2007), whereas the submillimeter wave polarimetry was placed on an equivalent extinction polarimetry scale using Equation 6. For the outer part of the cloud, we find an exponent for the fractional polarization consistent with earlier studies. However, we find a change in the exponent from  $b \approx 0.6$  to 1.0 at an extinction of  $A_V \sim 20$  mag (Figure 10a; B-G Andersson, J.A. Acosta Pulido, J.E. Vaillancourt, M. Charcos Llorens, S.S. Shenoy, in preparation), indicating that the alignment is lost beyond this depth.

Total elemental abundance constraints require an upper cutoff of the grain size distribution in the  $a \approx 1$ –2- $\mu\text{m}$  range (Kim & Martin 1995). The observed break is consistent with an upper grain size cutoff of  $a = 2 \mu\text{m}$  (Kim & Martin 1995; Figure 11b) and the RAT condition for alignment ( $\lambda < 2a$ ). Following behavior described by a standard interstellar extinction curve, the cloud becomes opaque to this radiation,  $\tau(4\mu\text{m}) = 1$ , at extinction levels of  $A_V \gtrsim 21$  mag (for  $R_V = 5$ ) or  $A_V \gtrsim 24$  mag (for  $R_V = 3.1$ ). Therefore, the break point in the high-opacity polarization can be used to constrain the upper grain size cutoff.

Alves et al. (2014) performed a similar study in the Pipe nebula (Figure 10b) and also find a distinct break in the fractional polarization between the optical ( $b = 0.76 \pm 0.14$ ) and submillimeter data ( $b = 0.92 \pm 0.17$ ). They interpret the steep slope of the 870- $\mu\text{m}$  data as indicating the detection of a polarization hole—i.e., the loss of alignment at large opacities. Their NIR data also show a steep slope ( $b = 1$ ) in the outer parts of the cloud that then flattens ( $b = 0.34 \pm 0.03$ ) at  $A_V \approx 10$  mag. Given the very low implied turbulence in the Pipe nebula (Alves et al. 2014), this may correspond to the predicted behavior of the fractional polarization for a highly uniform magnetized cloud (Section 3.1; Jones et al. 1992).

## 3.2. Wavelength Dependence of the Polarization

The wavelength dependence of the UV-optical-NIR polarization is a powerful tool for probing grain alignment because the polarization curve can be used to estimate the size distribution of aligned grains (Mathis 1986, Kim & Martin 1995, Draine & Fraisse 2009). Because polarization results from differential extinction (Equation 3), the normalized polarization curve (for a fixed aligned grain size distribution) varies across the visible much less than the change in the total

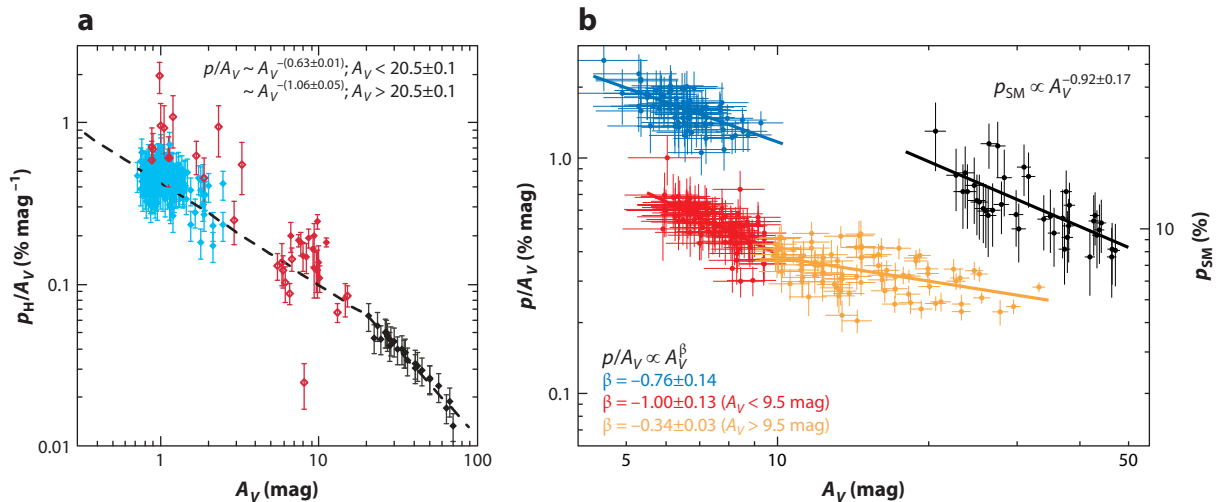


**Figure 10**

(a) Combining the fractional polarization efficiency from optical (cyan), near-IR (NIR) (red; Clemens et al. 2012 and B-G Andersson, J.A. Acosta Pulido, J.E. Vaillancourt, M. Charcos Llorens, S.S. Shenoy, in preparation) and 850  $\mu\text{m}$  (black; Crutcher et al. 2004) yields a break in the power-law exponent from  $-0.6$  to  $-1.0$  at  $A_V = 20.5$  mag in the LDN 183 cloud. At optical and NIR wavelengths the plotted efficiency follows directly from the measured values of  $p/A_V$ . At 850  $\mu\text{m}$  the plotted efficiency follows from  $p$  and has been put on the equivalent extinction scale by converting the intensity into optical extinction ( $p_{\text{ext}} = \tau p_{\text{emit}}$  and  $I_v = \tau B_v(T)$ ; also see Equation 6). The 850- $\mu\text{m}$  polarization has been scaled by a constant offset to match the NIR data at similar extinction values (near  $\sim 20$  mag), thereby allowing for variable, unknown grain temperatures and emissivities. Reprinted from Lazarian et al. (2015) with permission.

(b) Alves et al. (2014) probed the Pipe-109 cloud with optical (blue), NIR (red and orange) and 870- $\mu\text{m}$  (black) polarimetry. They fit each set of fractional polarization separately, finding a slope similar to that in LDN 183 for the submillimeter fractional polarization ( $p_{\text{SM}}$ ) at  $A_V > 20$  mag. The flattening of the  $p/A_V$  slope at  $A_V \sim 10$  mag could indicate the radiative transfer effects predicted by Jones et al. (1992). Reproduced from Alves et al. (2014) with permission © ESO.

opacity (less than  $\sim 15\%$ ) between  $A_V = 0.1$  mag and 10 mag (cf. Jones 1989; Section 3.1). Therefore, the polarization curve has an advantage over single-wavelength observations in that its shape (parameterized by  $\lambda_{\text{max}}$  and  $K$ ) is insensitive to the magnetic field topology and turbulence in the cloud (see the sidebar, Polarization Reduction Factors). This argument applies even more strongly in the FIR/millimeter band in which the opacities are much smaller.

As originally proposed by Davis & Greenstein (1951) both the spin-up and randomization of the grains are driven by collisions with the gas. The theory then predicts that the alignment efficiency should decrease with grain size and that grains with  $a > 0.1 \mu\text{m}$  should not be aligned (cf. Draine 2011). However, inversion of the interstellar extinction and polarization curves (Kim & Martin 1995) shows that the opposite is true (**Figure 11b**); grains with  $a \leq 0.05 \mu\text{m}$  are not aligned, whereas grains with  $a > 0.1 \mu\text{m}$  are well aligned.

UV polarization provides information on the alignment of the smallest grains. Only a small fraction of observed lines of sight exhibit a significant UV polarization, relative to the standard Serkowski curve for diffuse lines of sight (Clayton et al. 1995, Anderson et al. 1996). Some of these sightlines may also show polarization in the 2175-Å extinction feature. Although the inversion of the polarization curves for typical diffuse ISM sightlines indicates an abrupt small-size cutoff of the aligned grains at  $a = 0.04\text{--}0.05 \mu\text{m}$ , the distribution of aligned grains extends to much smaller sizes for these sightlines (Kim & Martin 1995; **Figure 11b**). The diffuse ISM cutoff in the size distribution of aligned grains is consistent with the RAT alignment criterion  $\lambda < 2a$ , and the Lyman limit ( $\lambda > 912 \text{ Å}$ ) of the general ISM radiation field. For the targets in which enhanced UV

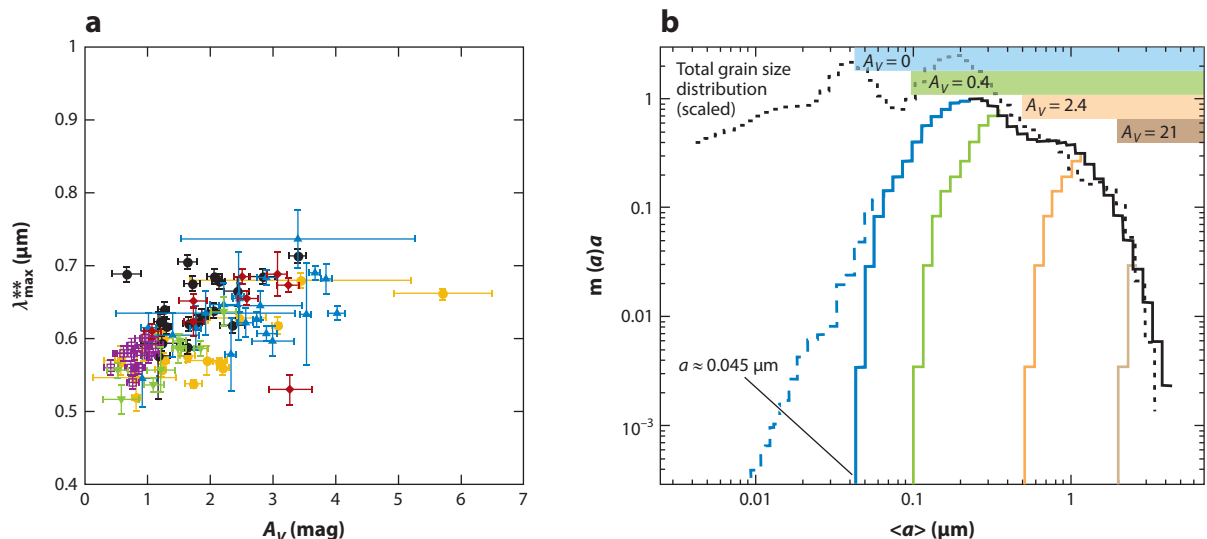


**Figure 11**

(a) The wavelength of maximum polarization,  $\lambda_{\max}$ , is correlated with the extinction,  $A_V$ . Different color points correspond to data from different nearby clouds. The data for each cloud have been shifted vertically to account for the different average grain sizes (via  $\langle R_V \rangle$ ), such that  $\lambda_{\max}(A_V = 0) = (0.166 \pm 0.003) \cdot R_V$ . (For plotting purposes the dispersion in the observed values of  $\lambda_{\max}$  have also been corrected for varying levels of measured high-mass star formation in each cloud, as indicated by the notation  $\lambda_{\max}^{**}$ ; see Andersson & Potter 2007 for details.) Reproduced from Andersson & Potter (2007) with permission of the AAS. (b) Kim & Martin (1995) inverted the interstellar extinction and polarization curves to estimate the total (black dotted line) and aligned (solid lines) grain-mass distributions. They find that the larger grains are better aligned and that the small-size cutoff for aligned grains in the diffuse ISM is  $a \approx 0.045 \mu\text{m}$ . Only for those sightlines showing polarization in the 2175-Å extinction feature are smaller grains aligned (blue dashed line). The green, red, and maroon curves are schematic cutoffs based on the radiative alignment torque condition  $a = \lambda/2$  for the  $A_V$  values shown. Adapted from Kim & Martin (1995) with permission of the AAS.

polarization indicates aligned grains smaller than  $0.04 \mu\text{m}$ , localized sources of short wavelength radiation may intersect the line of sight to the background star. Such enhanced illumination is also expected to result in a higher dust temperature. However, as noted in Section 2.1.2, Clayton et al. (1995) report enhanced 60- $\mu\text{m}$  emission only toward HD 197770 in their sample of stars with enhanced UV polarization. Further work is required to address whether this is due to the relatively poor sensitivity and spatial resolution of early FIR surveys or whether the UV polarization excess is due to paramagnetic alignment.

More generally, the polarization curve parameters, in particular  $\lambda_{\max}$ , have been used to probe grain alignment variations. Whittet et al. (2001) found a correlation of  $\lambda_{\max}$  with  $A_V$  for lines of sight probing Taurus and Chamaeleon I, albeit with somewhat poor statistical significance owing to a number of outliers. Andersson & Potter (2007) extended this work to include six nearby cloud complexes (Chamaeleon, Musca, Ophiuchus, the R CrA cloud, the Southern Coalsack, and Taurus) and found a well-defined correlation between  $\lambda_{\max}$  and  $A_V$  (Figure 11a). Comparing visual extinctions with 60- to 100- $\mu\text{m}$  color temperatures for large samples of field stars in each cloud, they showed that the outliers in this  $\lambda_{\max}$ - $A_V$  relation were toward targets for which the line-of-sight extinction was not an accurate measure of the radiation field experienced by the dust grains.

With the tighter distribution of measurements they were able to show that though the slope of  $\lambda_{\max}$  versus  $A_V$  is universal for the clouds studied, its normalization,  $\lambda_{\max}(A_V = 0)$ , is proportional

to the average value of the total-to-selective extinction,  $R_V$ , in each cloud. In contrast with Whittet & van Breda's (1978) findings, Andersson & Potter did not see a direct dependence of  $\lambda_{\max}$  on  $R_V$  within each cloud, although they recover the former result when combining all data sets. Because  $R_V$  is determined by the average grain size (Kim et al. 1994), they interpreted this to signify that the polarization curve, and specifically  $\lambda_{\max}$ , is the result of a convolution between the total grain size distribution and a radiative alignment driving.

In the RAT paradigm, variations in  $\lambda_{\max}$  are naturally tied to variations in visual extinction via the alignment requirement of  $\lambda < 2a$ . As light traversing regions of higher extinctions is progressively reddened, the small-grain cutoff for alignment grows with  $A_V$  (**Figure 11b**), yielding the observed  $\lambda_{\max}$  versus  $A_V$  correlation. To account for a possible role of the balancing disalignment, we note that the gas-grain collision rate scales as  $(nT^{1/2})_{\text{gas}}$ . Because the gas temperature and density are expected to be anticorrelated in interstellar clouds, the collision rate likely varies slowly. It is straightforward to show that for thermally rotating grains the disalignment timescale is proportional to the grain size and, thus, that the smallest grains disalign first (Whittet 2003). Suprathermally rotating grains are, to first order, impervious to thermal collisions. Thus, if important, collisional disalignment implies that the alignment driving must be fastest for those regions with the smallest values of  $\lambda_{\max}$ —that is, at small  $A_V$ —supporting RAT alignment.

Finally, assuming a fixed upper grain size but a varying small size cutoff, depending on the available minimum wavelength, the center ( $\lambda_{\max}$ ) and width ( $K$ ) of the polarization curve should be correlated, as has been observed by Wilking et al. (1980) and Whittet et al. (1992). If significant grain growth is taking place, a more complex relationship for  $\lambda_{\max}$  versus  $A_V$  and  $\lambda_{\max}$  versus  $K$  may be expected. Relatively few observational data exist for the Serkowski curve beyond extinctions of  $A_V = 2\text{--}4$  mag. However, Ysard et al. (2013) have argued, on the basis of the combined analysis of NIR extinction and FIR photometry, that grain coagulation must be taking place in Taurus and is dependent on space density rather than extinction. Preliminary data from J.E. Vaillancourt, B-G Andersson, D.P. Clemens, and E.E. Becklin (in preparation) indicate that the  $\lambda_{\max}$  versus  $A_V$  relation may bifurcate beyond this extinction.

Emission polarization in the FIR shows a decrease with wavelength up to  $\sim 350\text{ }\mu\text{m}$ , followed by a rise at longer wavelengths (Vaillancourt et al. 2008; **Figure 2b**). However, isothermal dust for most grain materials produces inherently flat polarization spectra for  $\lambda \gtrsim 50\text{ }\mu\text{m}$  (Hildebrand et al. 1999). As first shown by Hildebrand et al. (1999; cf. Vaillancourt 2002, 2007; Bethell et al. 2007), this discrepancy can be resolved by assuming a mixture of grains with differing emission/absorption cross sections. For example, for a mix of aligned silicate and unaligned carbon dust, the larger UV absorption cross section of carbon grains (Mathis et al. 1983) makes these warmer than the silicate grains and results in a spectrum that rises with wavelength.

Draine & Fraisse (2009) performed a more quantitative modeling of carbon and silicate grain mixtures with a uniform spatial dust distribution and heating. Their predicted polarization spectrum, beyond  $\sim 350\text{ }\mu\text{m}$ , matches the observational trend (**Figure 2b**) of increasing polarization in cases in which only silicates are aligned.

Such a model cannot also explain the FIR polarization drop with wavelength at  $\lambda \sim 50\text{--}350\text{ }\mu\text{m}$ . However, because all clouds with well-established FIR polarization spectra contain embedded radiation sources, the observations must sample materials at different temperatures along the line of sight. Shorter wavelengths then successively sample warmer material closer to the embedded heating source. The falling polarization spectra at the shorter FIR wavelengths then indicate that the hotter dust is also better aligned. This strongly indicates radiative alignment, a hypothesis supported by the spatial distribution of the FIR polarization, as discussed below for the clouds W3 and M17 (Section 3.4).

### 3.3. Polarized Microwave Dust Emission

One expected consequence of spinning, charged grains is the emission of electric dipole radiation. For small grains/PAHs and typical interstellar conditions, the grains are likely to have a net charge, and such radiation is predicted to peak at microwave frequencies ( $\sim 10\text{--}100$  GHz; Draine & Lazarian 1998a,b; Hoang & Lazarian 2012). In addition, magneto-dipole emission of nanoparticles of strongly magnetic materials is a possibility (Draine & Lazarian 1999, Draine & Hensley 2012).

The existence of this spinning dust emission has been clearly confirmed by observations (e.g., Kogut et al. 2011, Planck Collab. XX 2011, Tibbs et al. 2012, Planck Collab. XV 2014) and is often referred to as the anomalous microwave emission (AME) because it could not initially be identified with typical microwave emission mechanisms. These grains are smaller than the size cutoff inferred from the inversion of the Serkowski curve (Section 3.2; **Figure 11b**) and are not expected to be well aligned by the RAT mechanism (Section 2.3.3). However, the process of “resonance paramagnetic relaxation” (Section 2.1.3) may weakly align these small grains, producing polarization levels as high as a few percent (Lazarian & Draine 2000, Hoang et al. 2013). The analyses for two stars with observed polarization in the  $2175\text{-}\text{\AA}$  extinction bump by Hoang et al. (2013) are consistent with these limits.

A single ( $3.6\sigma$ ) detection of polarization of the AME has been reported toward the Perseus molecular cloud (Battistelli et al. 2006), together with upper limits of a few percent in other regions (Rubio-Martín et al. 2012 and references therein), placing constraints on the alignment of this spinning dust. In addition, a comprehensive analysis of the polarization spectrum from the *Planck* data (Planck Collab. XXII 2015) shows no detected contribution from a polarized AME.

### 3.4. Enhanced Alignment Close to a Discrete Radiation Source

The results from Whittet et al. (2008; **Figure 9**) indicate, in a statistical sense, that the grain alignment is enhanced close to discrete radiation sources. Targeted observations support this result. For example, Andersson & Potter (2010) used multiband optical data to show that the alignment for background stars probing the dust around HD 97300 is enhanced at small projected distances to the star (**Figure 12a**). Cashman & Clemens (2014) have shown that the average fractional polarization in LDN 204 decreases systematically with increasing projected distance to  $\zeta$  Oph (**Figure 12b**).

A somewhat more indirect probe of the relationship between radiation field and grain alignment can be derived by comparing the dust temperature with the polarization and assuming that the dust heating is dominated by the radiation field. Matsumura et al. (2011) used multiband optical polarimetry and FIR dust temperatures to study a sample of stars in the Pleiades, in which the intense radiation field in the cluster allowed them to compare the wavelength-dependent fractional polarization with the color temperature of the dust. Combining their data with results from the literature, they show that the grain alignment is enhanced for warmer dust in several regions, showing a correlation between grain heating and alignment.

For most clouds with measured FIR/millimeter wave polarization, stellar densities are large enough that regions with and without embedded stars cannot be spatially separated with current data. However, some relevant information can be gleaned from polarization measurements toward OB star clusters powering HII regions.

One example is shown in **Figure 13**, in which the spatial distribution of the  $60\text{-}\mu\text{m}$  fractional polarization,  $p$ , appears to follow the distribution of several HII regions as delineated by thermal, 5-GHz emission (Wynn-Williams 1971, Schleuning et al. 2000). The OB stars ionizing the

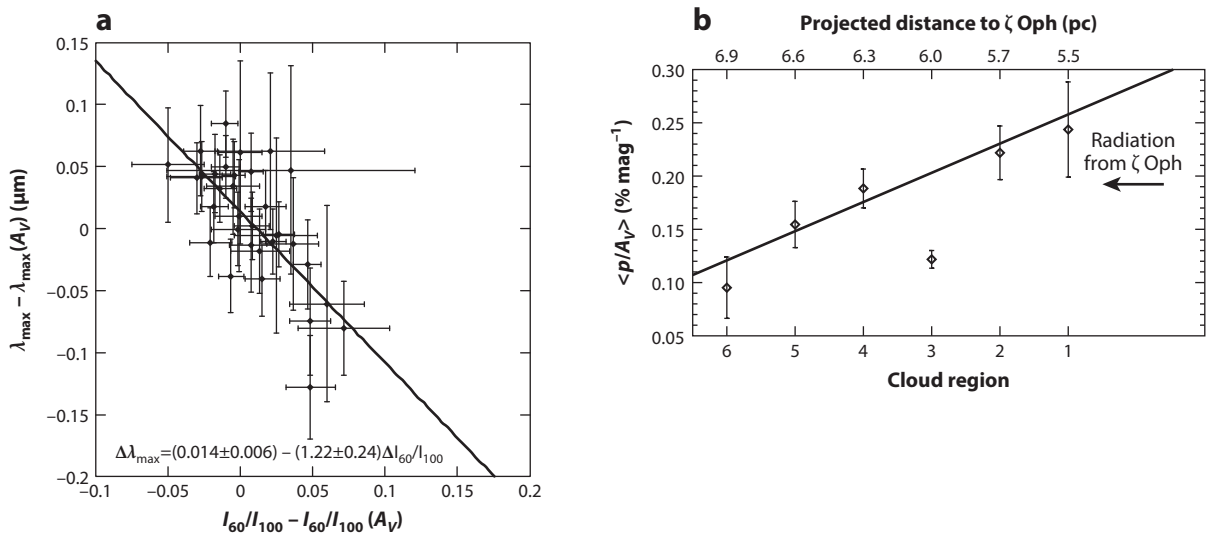


**Figure 12**

(a) The relative alignment efficiency is measured by the change in the location of the polarization curve peak,  $\lambda_{\max}$ , from the value predicted by the extinction along the line of sight,  $A_V$ . Dust heating is probed by the IRAS  $I_{60}/I_{100}$  color temperature. These values are anticorrelated for dust around the star HD 97300, indicating that as the dust is heated by the star, the alignment improves. Reproduced from Andersson & Potter (2010) with permission of the AAS. (b) Cashman & Clemens (2014) used Mimir  $H$ -band observations (Clemens et al. 2007) of more than 7,000 stars to probe the LDN 204 cloud in Ophiuchus. They show that the average fractional polarization  $p/A_V$  in six cloud regions with different projected distances from the O9.5 V star  $\zeta$  Oph has a systematic, linear enhancement with smaller distances to the star. Reproduced from Cashman & Clemens (2014) with permission of the AAS.

hydrogen and providing aligning torques to the dust must also be heating the grains. A comparison of both panels of **Figure 13** suggests that the spatial distribution of the 20- $\mu\text{m}$  total intensity traces the distribution of HII regions and radio data better than the 60- $\mu\text{m}$  total intensity data, as would be expected for dust heated to  $\gtrsim 70$  K (Salgado et al. 2012). Because the polarized intensity closely follows the total short-wave intensity, a correlation between the spatial location of warm grains and aligned grains is indicated.

The M17 HII region and its nearly edge-on photodissociation region (PDR) provide a test of alignment for nonuniform dust illumination (Zeng et al. 2013). Here, an OB star cluster has generated an HII region bounded by an expanding shock front in dense gas and dust. Beyond the shock front, the dust temperature is seen to drop. Zeng et al. probed the dust alignment variations in the region by splitting the cloud data into two regions separated by the PDR. They found that the submillimeter wave polarization spectrum fell from 350 to 450  $\mu\text{m}$  for the majority of points on the hot side of the PDR, with  $p(450 \mu\text{m})/p(350 \mu\text{m}) = 0.8 \pm 0.2$ , whereas for points beyond the shock, a rising spectrum with  $p(450 \mu\text{m})/p(350 \mu\text{m}) = 1.3 \pm 0.4$  is seen. These results support the interpretation of the FIR polarization spectrum by Vaillancourt et al. (2008) in which grains are warmer and better aligned near stars embedded in molecular clouds.

### 3.5. Temperature-Dependent Alignment

In addition to introducing the notion of superparamagnetism to enhance the DG alignment, Jones & Spitzer (1967) noted that—based on fundamental thermodynamic arguments—grains rotating with thermal energy angular momenta can only be aligned by paramagnetic alignment if the gas



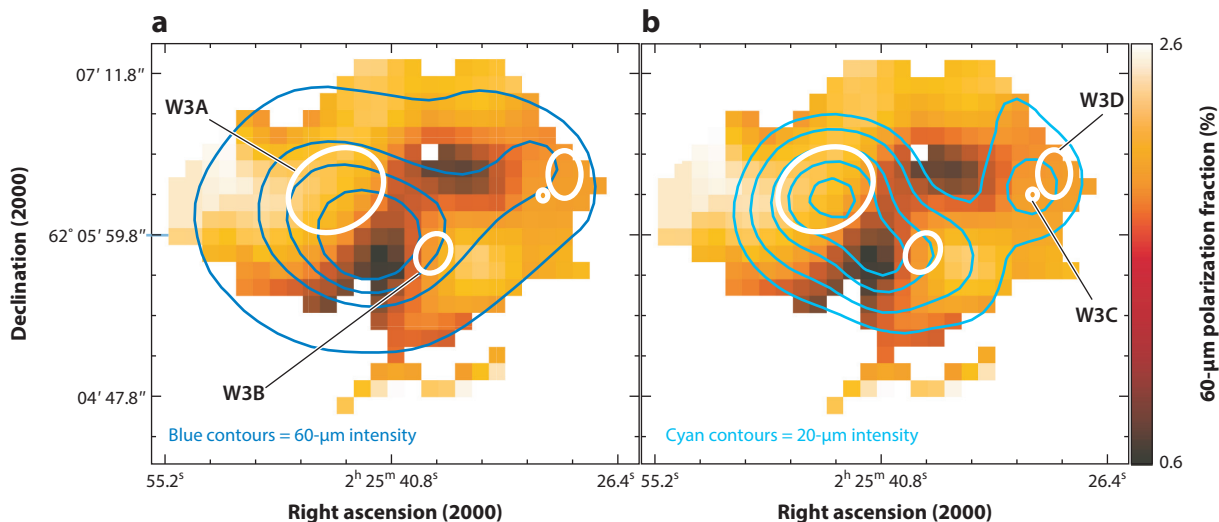


**Figure 13**

The 60-μm polarization fraction in the W3 molecular cloud (Dotson et al. 2000, Schleuning et al. 2000) is shown in color scale (*color bar* at *right*) in both panels. White contours show HII regions identified at 5 GHz (Wynn-Williams 1971). (a) The total unpolarized intensity at 60 μm is shown as blue contours at 20, 40, 50, 60, and 80% of the intensity peak ( $\sim 8$  kJy per 22-arcsec beam). The intensity and polarization data at 60 μm were measured simultaneously and have spatial resolution of  $\sim 37$  arcsec. (b) The 20-μm intensity as measured by MSX (e.g., Price et al. 2001, Egan et al. 2003), with a spatial resolution of  $\sim 20$  arcsec, is shown as cyan contours at 10, 20, 40, 60, and 80% of the peak intensity ( $\sim 80$  GJy  $\text{sr}^{-1}$ ).

and dust temperatures differ. The heating of the low-to-medium extinction ISM is dominated by photoelectric emission from grains, whereas the cooling is dominated by line radiation in the FIR/millimeter band (e.g., Mathis et al. 1983, Wolfire et al. 1995). As a result, the gas temperature should be both higher than the dust temperature at the surface of the clouds and vary more rapidly as a function of opacity. Models (e.g., Hollenbach et al. 2009) indicate that beyond  $A_V \approx 5$ –10 mag the gas and dust should equilibrate. Additionally, Roberge (1996) has argued, on the basis of observational constraints from Hildebrand & Dragovan (1995), that even in the limit of infinitely large superparamagnetic aligning torques the gas temperature must still be at least  $5 \times T_{\text{dust}}$  for thermally rotating superparamagnetic grains to be aligned. Hence, at large opacities paramagnetic alignment should fail (cf. Roberge & Lazarian 1999).

Jones et al. (1984) tested this prediction toward the densest, star-less (Kato et al. 1999) core in the Southern Coalsack ( $A_V \approx 15$  mag) by comparing deep *H*-band polarimetry with gas and dust temperature tracers. Based on CO ( $J = 1$ –0) observations by Huggins et al. (1977) and their own upper limits on the 135-μm continuum emission from the globule, Jones et al. estimated both the gas and dust temperatures to be  $\sim 10$  K. They further showed that the position angles of the polarization toward the core of the cloud differed systematically from the surrounding fields. Although some stars in the Jones et al. sample may partially probe Carina arm material (Andersson & Potter 2005), the systematic difference in position angle between the core of the cloud and the general Coalsack indicates that polarization is originating in the core. Therefore, dust grains are aligned deep in the globule, in conflict with predictions of (super)paramagnetic alignment.

A more direct test of alignment at high opacities was performed by Chrysostomou et al. (1996) and in particular Hough et al. (2008). They used the polarization in spectral features of interstellar ices, most importantly the CO ice line at 4.67 μm, to sample material deeply embedded in clouds.

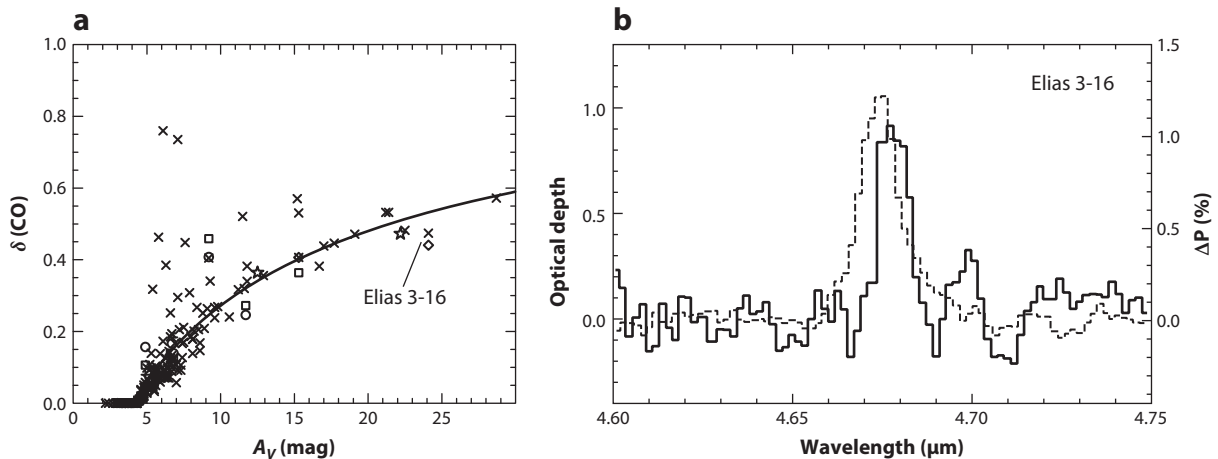


**Figure 14**

(a) The ratio  $\delta\text{CO} [= N(\text{CO})_{\text{solid}}/N(\text{CO})_{\text{total}}]$  shows an abrupt onset in column density at  $A_V \approx 7$  mag, yielding a rise in the solid phase CO toward larger opacities, due to the freeze out of the gas onto dust grain mantles. Reproduced from Whittet et al. (2010) with permission of the AAS. (b) The strong line polarization signal (solid line) in the CO ice line at  $4.67 \mu\text{m}$  shows that grains are aligned at large opacities. The dotted line represents the Stokes I line opacity. Reproduced from Hough et al. (2008) with permission.

As shown by Whittet et al. (1989, 2010) the column density of solid CO has an abrupt onset at  $A_V = 6.7 \pm 1.6$  mag, usually interpreted to mean that ice mantles (photo)desorb at lower opacities (cf. Boogert et al. 2015 in this volume). Additionally, observations taken by Whittet et al. (2010; **Figure 14a**) indicate that the fractional abundance of CO in the solid phase rises continuously to larger opacities, reaching 50% only at  $A_V \approx 20$  mag. Thus, the effective visual extinction for an observed CO ice line is significantly larger than the onset opacity. Comprehensive models of the structure in a dark cloud (Hollenbach et al. 2009) show that even with an elevated radiation field, the gas and dust temperatures approach each other at opacities in which CO ice formation starts and have only a  $\sim 1$ -K difference at  $A_V \approx 10$  mag. Hence, significant CO ice abundance is reasonably associated with low absolute and near-equivalent gas and dust temperatures.

Hough et al. (2008) probed the CO ice polarization toward the true background star Elias 3-16 in Taurus ( $A_V = 24.1 \pm 0.4$  mag). The strong polarization seen (**Figure 14b**) shows that grains are aligned in regions at least as deep as  $A_V \approx 10$  mag.

### 3.6. Angle-Dependent Alignment Efficiency

A unique prediction of RAT theory is that the grain alignment efficiency should depend on the angle between the magnetic field and the radiation field anisotropy,  $\Psi$  (**Figure 15a**), because the radiation is responsible for both the spin-up of the grain and the alignment with the magnetic field. This prediction can be tested by comparing the polarization toward background stars with the azimuthal angle  $\Psi'$  about an aligning star, in which  $\Psi'$  is the projection of  $\Psi$  onto the plane of the sky (**Figure 15a**). Although generally  $\Psi' \neq \Psi$ , any periodic variation of  $\Psi'$  must still result from a periodic variation in  $\Psi$ . Andersson et al. (2011) performed such a test around the star HD 97300 illuminating the Chamaeleon I cloud (**Figure 15b**). HD 97300 is sufficiently close to the cloud ( $\sim 0.03$  pc; Andersson & Potter 2010) that the difference between  $\Psi'$  and  $\Psi$  is small, particularly because the alignment shall be strongest at the cloud surface closest to the

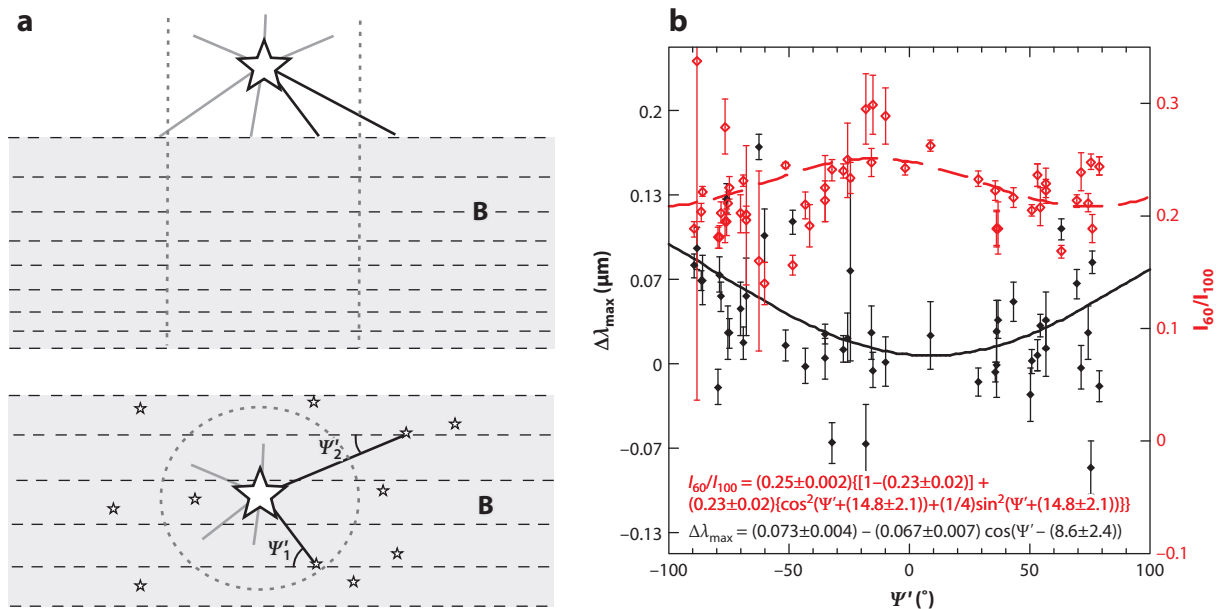


**Figure 15**

(a) The predicted angle dependence of radiative alignment can be probed where a discrete source (*star*) is located close to a cloud and dominates the radiation field incident upon the grains. HD 97300, located near the surface of the Chamaeleon I cloud, provides such a geometry. The upper panel shows the exciting star outside of the actual dust cloud as viewed face on, with magnetic field **B** threading the cloud. The lower panel shows the relative geometry when viewed along the line of sight, including the background star lines of sight (*small stars*). (b) Alignment efficiency toward background stars, as traced by  $\Delta\lambda_{\max}$ , as a function of  $\Psi'$  (*black points*) is compared with the far-IR color temperatures ( $I_{60}/I_{100}$ ) toward the same background star (*red points*). A decrease in  $\Delta\lambda_{\max}$  corresponds to enhanced alignment. Solid and dotted lines show best fits to a sinusoidal relation, with fit parameters as shown in the equations. Reproduced from Andersson et al. (2011) with permission from A&A, © ESO.

star (**Figure 12a**). Using the offsets from the nominal  $\lambda_{\max}$  ( $A_V$ ) relation for the cloud (where a smaller  $\Delta\lambda_{\max}$  corresponds to enhanced alignment), they found a local minimum versus  $\Psi'$  with a signal amplitude of  $9\sigma$  significance centered at  $\Psi' = 9 \pm 3^{\circ}$ , which is close to the theoretical prediction of  $\Psi' = 0$ . (No systematic variation in polarization position angle was detected with respect to  $\Psi'$ .) Other variations in the true angle  $\Psi$  that are not represented by  $\Psi'$  may result from line-of-sight integration through the cloud thickness and from the projected radial distance between the background and exciting stars. However, these effects only produce additional scatter in the data and, thus, tend to lower the amplitude of the observed polarization versus  $\Psi'$  signal.

This polarization result can be indirectly tested by comparing it to the color temperature of the dust. Assuming oblate grains whose heating is proportional to the surface area exposed to the starlight (and isotropic radiative cooling), the IRAS  $I_{60}/I_{100}$  ratio indicates a grain temperature variation that varies as a function of  $\Psi'$  in a way that is consistent with the polarimetry results (**Figure 15b**).

A similar result is seen in FIR polarization data within 1.5 arcmin of the Becklin-Neugebauer object in Orion. Using archival data (Dotson et al. 2000, 2010; Matthews et al. 2009), J.E. Vaillancourt & B-G Andersson (in preparation) find a distinct enhancement of alignment efficiency with  $\Psi'$  at 100  $\mu\text{m}$  centered on the average magnetic field direction. A detection with a smaller relative amplitude, in the same direction, is also made at 350  $\mu\text{m}$ . This trend of falling signal significance with increasing wavelength indicates that the hotter dust is better aligned. Although

the density, and hence the internal opacity, in the BN/KL object is large, it is important to remember that the RAT alignment condition implies that, if the upper grain size limit in the nebula is as small as  $a_{\text{max}} = 1 \mu\text{m}$ , radiation with  $\lambda < 2 \mu\text{m}$  shall allow alignment. Even longer illuminating wavelengths can generate alignment for larger  $a_{\text{max}}$ , especially if grain growth has taken place.

### 3.7. The Effects of Mineralogy

In the paramagnetic alignment mechanism, the alignment efficiency of a grain increases with increasing magnetic susceptibility of the material. Therefore, enhanced polarization should be achieved for grains containing inclusions of high-susceptibility compounds (Jones & Spitzer 1967), specifically of small ferromagnetic subgrains embedded in the bulk silicate grain (Jones & Spitzer 1967, Mathis 1986). Based on this assumption, Mathis (1986) showed that the Serkowski polarization curve could be reproduced with a standard overall power-law grain size distribution (Mathis et al. 1977) and the assumption that a (silicate) grain is aligned if it contains at least one such superparamagnetic inclusion. The identification of glass with embedded metals and sulfides (GEMS) grains in interplanetary dust particles from comets (Bradley 1994, Bradley et al. 2000) lent support to this hypothesis. These GEMS contain Fe(Ni) metals and iron-rich sulfides, have sizes consistent with the theory of Mathis, and exhibit superparamagnetic susceptibilities (Bradley 1995, Goodman & Whittet 1995).

Voshchinnikov et al. (2012) performed an important test of the effects of dust mineralogy on grain alignment. Combining a sample of 196 lines of sight with high-quality depletion measurements in Si, Mg, and Fe with polarimetry and extinction data, they searched for variations in the fractional polarization with depletion patterns. By assuming that all depleted (solid phase) silicon atoms are incorporated into materials with the stoichiometry of olivine (a moderately paramagnetic mineral), they could probe for enhanced alignment in higher-susceptibility grains. The remaining solid-phase iron provides the reservoir available for superparamagnetic forms of iron-bearing minerals, in accord with the GEMS inclusions probed by Bradley (1994). Voshchinnikov et al. then searched for evidence for superparamagnetic alignment by comparing the observed fractional polarization with the relative abundance of the “remaining” solid-phase iron. In a subsample of 95 lines of sight, no correlation is seen (**Figure 16**), indicating that superparamagnetic alignment is likely not a significant mechanism for larger grains (cf. Section 2.3.4).

The strong polarization seen in the 9.7- $\mu\text{m}$  and 18- $\mu\text{m}$  silicate spectral features (Smith et al. 2000) shows that silicate grains are aligned. In contrast, sensitive searches for polarization in the 3.4- $\mu\text{m}$  line of the aliphatic C–H stretch mode do not show detectable polarization (e.g., Chiar et al. 2006). As a result of the exposure to atomic hydrogen and UV photons, such surface groups are expected to be present on all forms of carbonaceous dust in the diffuse ISM (Chiar et al. 2013 and references therein). Thus, the lack of polarization in this spectral feature indicates that carbon grains are not aligned. This is supported by the fact that in models of the FIR-to-submillimeter polarization spectra by Draine & Fraisse (2009), only those assuming spherical carbon grains (equivalent to nonalignment) match the observations (Vaillancourt & Matthews 2012; Section 3.5). The spectral dependence of the submillimeter-to-millimeter polarization determined by the *Planck* project is also consistent with this interpretation (Planck Collab. XXII 2015). Additionally, comparisons of linear and circular polarization in the ISM indicate that the grains responsible for the polarization are good dielectrics (Martin 1974, Martin & Angel 1976, Mathis 1986). This is a characteristic consistent with silicate dust but not with carbonaceous grains.

In the RAT paradigm, this dichotomy between silicate and carbonaceous grain alignment can be understood by noting that, whereas the grain spin-up is solely dependent on the grain helicity and scattering characteristics, the alignment requires a paramagnetic susceptibility large enough to

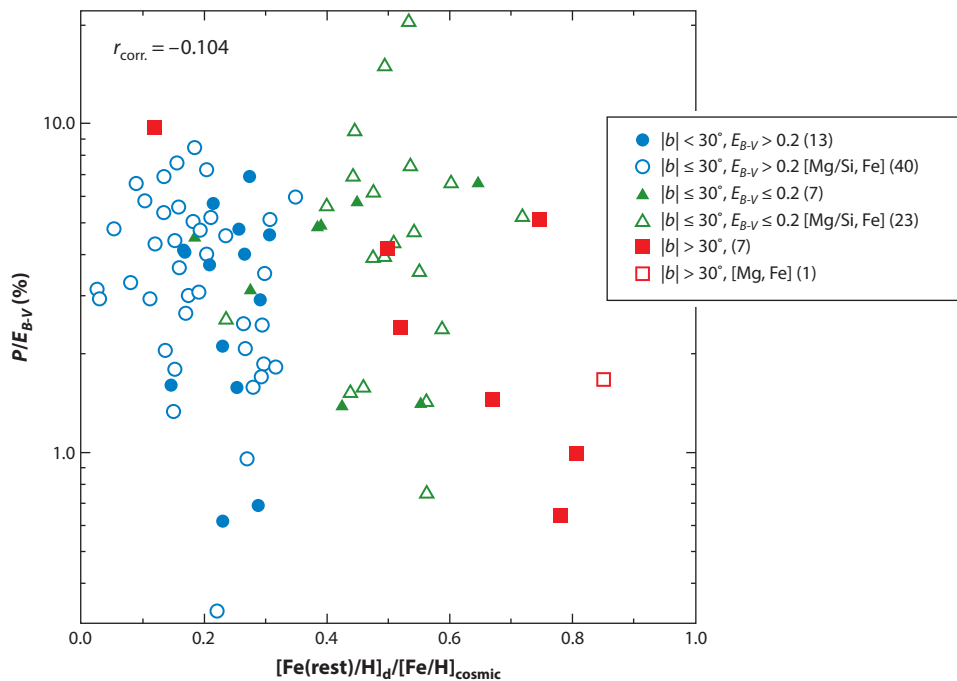


**Figure 16**

Voshchinnikov et al. (2012) used depletion data for Si, Mg, and Fe for a large number of lines of sight to estimate the amount of iron in a superparamagnetic/ferromagnetic form  $[\text{Fe}(\text{rest})]$ . They compared this mineralogical parameter with the fractional polarization,  $P/E_{B-V}$ , to probe for superparamagnetic alignment. No statistically significant correlation was found. Reproduced from Voshchinnikov et al. (2012) with permission from A&A, © ESO.

generate a Barnett magnetization in the spinning grain, thus causing Larmor precession around the magnetic field lines. Because carbon forms diamagnetic materials, such grains may not experience a significant Barnett magnetization. The behavior and relative contribution to the polarization by composite grains shall require detailed modeling.

In a small number of lines of sight, the 2175-Å extinction bump shows associated polarization (Clayton et al. 1995, Anderson et al. 1996, Martin et al. 1999). This extinction feature is often attributed to small graphite grains or PAHs (e.g., Steglich et al. 2011). Therefore, these may be aligned, at least in some environments, even if the larger amorphous carbon grains required by models (Clayton et al. 2003, Draine & Li 2007) are not. Small sheets of graphene (equivalent to large PAHs) have recently been predicted to display significant Pauli paramagnetism (Ominato & Koshino 2012), which may yield sufficient Barnett magnetization to allow RAT alignment. Paramagnetic alignment (and resonance paramagnetic alignment) may also become efficient for the very small grain carriers of the 2175-Å bump (Hoang et al. 2014; Section 2.1.3). Observational tests of such alignment must be analyzed in the context of the mechanism in which PAH molecules can show polarized emission near a strong UV source owing to their orientation-dependent absorption cross section (Léger 1988, Sironi & Draine 2009). So far, only a single, marginal detection of polarization ( $0.86 \pm 0.28\%$ ; Sellgren et al. 1988) has been reported for the 3.3-μm feature attributed to PAHs in the Orion Bar (at a significantly higher level than predicted by Sironi & Draine:  $\sim 0.06\%$ ).

### 3.8. Pinwheel Torque (Enhanced) Alignment

As discussed in Section 2.3.4, molecular hydrogen formation may provide systematic torques, which could enhance the grain alignment whether in the paramagnetic or RAT paradigm. In most interstellar environments a chemical statistical equilibrium can be assumed to apply on timescales that are short compared with cloud evolution, specifically for the  $\text{H}_2$  abundance, such that for each molecule formation a balancing destruction must take place.

The direct dissociation of  $\text{H}_2$  requires a photon of  $E > 14.7$  eV (Stecher & Williams 1967), significantly beyond the ionization energy of atomic hydrogen ( $E = 13.6$  eV). Therefore, such photons are not expected to be available in the general ISM. The photodestruction of  $\text{H}_2$  instead takes place through a two-step process initiated by the photoexcitation of the molecule's electronic structure (Field et al. 1966). If, upon relaxation into the ground electronic state, the molecule has a vibrational state of  $v = 14$  or higher (at a branching ratio of  $\sim 15\%$ ), vibrational dissociation follows (Draine 2011). The initial excitation into the electronically excited state requires a photon with  $\lambda < 1108$  Å. Assuming a standard interstellar extinction curve, and ignoring the self-shielding in the  $\text{H}_2$  spectral lines (e.g., Federman et al. 1979),  $\tau(1108 \text{ Å}) = 1$  is reached at  $A_V \approx 0.25$  mag, which is well below any observed break in the grain alignment efficiency (e.g., **Figures 9 and 10**).

Similar arguments apply to the viability of spin-up torques caused by photoelectric emission from the grains. As noted above (Section 3.1), the photons required for such electron emission are excluded at  $A_V > 0.5$  mag. Hence, unless the cloud material is highly porous, Purcell alignment should not be active beyond approximately one magnitude of visual extinction.

Sorrell (1995) proposed that cosmic-ray-driven evaporation of grain mantles could drive grains at deeper levels to suprathermal spin velocities. However, Lazarian & Roberge (1997b) argued that this mechanism required cosmic ray fluxes 6–7 orders of magnitude larger than expected in molecular clouds.

Although high magnetic susceptibility or suprathermal rotation does not seem to allow alignment through paramagnetic relaxation, these effects may nonetheless contribute to grain alignment by enhancing the efficiency of radiative alignment (Hoang & Lazarian 2009a). When “pinwheel” torques (from ejection of  $\text{H}_2$  or electrons) are added to the radiative torques, they are predicted to lift the grains out of low angular momentum states (Section 2.3.4), thereby allowing the RAT process to achieve more efficient alignment.

To probe the effect of pinwheel torques, Andersson et al. (2013) investigated the polarization properties toward stars behind the reflection nebula IC 63 (Jansen et al. 1994, 1995; Luhman et al. 1997; France et al. 2005; Andersson et al. 2013). Eighty-five percent of electronic photoexcitations that initiate photodestruction of the molecule relax to the ground state. The resulting fluorescent cascade (Draine 2011) can be used to trace the photodestruction rate of the molecule. Because the dynamical timescale of the PDR is long compared with the destruction and reformation time of the molecule (Tielens 2005, Morata & Herbst 2008), the fluorescent rate also traces the formation rate of the molecule. Andersson et al. found that the measured polarization increased with increasing fluorescent intensity across the nebula in a linear manner (**Figure 17**), with one significant outlier point. Based on the  $\text{HCO}^+$  observations by Polehampton et al. (2005), they argue that this line of sight (star IC 63 #46) probes a region of strongly enhanced collisional disalignment (additional observations support this conclusion). As noted in Section 2.3.4, RAT predicts that alignment for superparamagnetic grains should be perfect, with no room for improvement from other mechanisms. Hence, the enhancement observed with respect to  $\text{H}_2$  formation torques suggests that most grains are not strongly superparamagnetic.



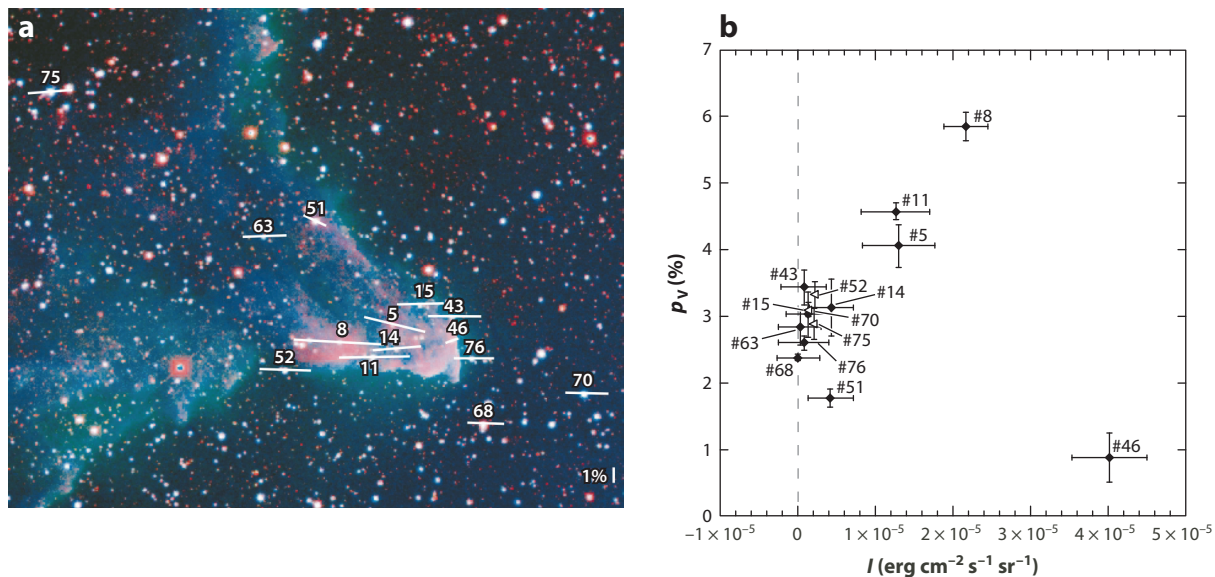


**Figure 17**

(a) The reflection nebula IC 63 shown in a false color image with  $\text{RGB} = \{\text{H}_2 \text{ 1-0 S(1), POSS2 Red, POSS2 Blue}\}$ . Visible polarization vectors are shown as white lines. (b) The amplitude of polarization toward IC 63 correlates well with the fluorescent intensity. The correlation shows that H<sub>2</sub> formation torques enhance the radiative alignment. Target #46, a clear outlier to the correlation, is localized behind the compression ridge at the front of the nebula in which the collisional disalignment is strongly enhanced and outweighs the alignment. Both panels adapted from Andersson et al. (2013) with permission of the AAS.

### 3.9. Possible Mechanical Alignment

In its most straightforward form (and as originally proposed by Gold 1952a,b), mechanical alignment in a magnetized medium yields an orientation of the polarization that is perpendicular to the projected field, because bulk motion in the ISM is generally restricted to flow along the magnetic field lines. Mechanical alignment driven by Alfvén waves or cyclotron motion has so far not been seen. However, the mechanism may be active in the innermost outflow regions of high-mass YSOs. For example, position angle rotations of  $\sim 90^\circ$  are sometimes seen along and across the molecular outflow direction in high spatial resolution polarimetry. This has been observed in the Kleinman-Low object (Rao et al. 1998), NGC 2071 (Cortes et al. 2006), and G5.89–0.39 (Tang et al. 2009). These results may indicate mechanical alignment in high flow-speed jets or may simply indicate the presence of complex field geometries near the protostellar sources. It is not clear if mechanical alignment can overcome the much stronger RAT alignment in these circumstances, and answering this question shall require detailed observation and modeling. Utilizing synchrotron emission from a YSO jet (e.g., Carrasco-González et al. 2010, 2011) could allow an independent determination of the magnetic field structure and test the viability of mechanical alignment in these environments.

## 4. CONCLUSIONS

Recent decades have seen remarkable convergence of theory and observations in the understanding of interstellar grain alignment. Theoretically, a quantitative, predictive theory, based on radiative

torques, has been developed and verified against numerical studies (Dolginov & Mytrophanov 1976; Drain & Weingartner 1996, 1997). The introduction of the analytical RAT model by Lazarian & Hoang (2007a) allows the theory to be applied, efficiently, to a range of realistic astrophysical situations and provides specific predictions amenable to observational testing.

A preponderance of observational data, from the UV to millimeter wave, now supports the RAT mechanism as the dominant process for aligning large ( $a > 0.05 \mu\text{m}$ ) interstellar grains (see **Table 1**). Paramagnetic alignment is inefficient for the large grains and is ruled-out as an alignment mechanism in molecular clouds. However, it may still dominate the alignment for very small grains/PAHs, which are responsible for the far-UV polarization and the 2175-Å bump in the extinction curve. Similarly, in most instances, mechanical alignment does not appear to be significant, but may contribute in specific situations such as in protostellar jets.

A quantitative, observationally supported grain alignment theory allows new and improved probes of magnetic fields and grain characteristics, such as mineralogy, size distribution, and emissivity. For example, the loss of alignment in deep star-less cores implies that polarization only probes the magnetic field at the cloud surface while providing a measurement of the large grain size cutoff. Additionally, multiwavelength observations support the hypothesis that the silicate dust is significantly better aligned than carbonaceous grains.

## 5. SOME REMAINING CHALLENGES AND POSSIBILITIES

Grain alignment physics has seen significant progress, opening up important new possibilities in astrophysics, but many challenges still remain. To use the predictive power of RATs, new observational capabilities and associated modeling are required. Large-scale surveys combined with deep, multiwavelength, targeted observations promise to enhance studies of the magnetic fields as well as dust and ISM characteristics. Exciting possibilities include the following:

- Observationally quantifying the details of RAT alignment shall refine the theory and provide better tools for studying the ISM, including magnetic fields and dust characteristics.
- In the FIR/millimeter band, several new opportunities are on the horizon, including balloon-borne (e.g., BLASTpol; Dober et al. 2014) and air-borne (e.g., SOFIA/HAWC; Dowell et al. 2010) instruments, that shall allow studies of dense clouds and provide new constraints on the poorly known temperature and emissivity variations of the grain alignment.
- The alignment process for the very smallest grains ( $a < 0.01 \mu\text{m}$ ) remains unsettled; both RATs from photons beyond the Lyman limit and paramagnetic alignment are good candidates. The limited existing sample of UV polarimetric observations poses a severe limitation on the understanding of this alignment. New UV polarimetry capabilities are needed to explore and use this aspect of grain alignment.
- Understanding the physics of the spinning dust/PAHs and its associated microwave emission shall allow a more secure characterization of the Galactic contribution to studies of the CMB radiation.
- The processes randomizing the grain orientations must be quantitatively explored in varying environments, including the ionized medium, and can provide new information about the dust and its environment.

## DISCLOSURE STATEMENT

The authors are not aware of any affiliations, memberships, funding, or financial holdings that might be perceived as affecting the objectivity of this review.

## ACKNOWLEDGMENTS

A substantial number of our colleagues provided comments and inputs on this review. We particularly want to acknowledge Thiem Hoang, Terry Jones, Doug Whittet, Bruce Draine, and Chris McKee for helpful suggestions and reading and commenting on various parts of the draft. We gratefully acknowledge support from the National Science Foundation through grant AST-1109469.

## LITERATURE CITED

- Abbas MM, Craven PD, Spann JF, et al. 2004. *Ap. J.* 614:781
- Alves FO, Frau P, Girart JM, et al. 2014. *Astron. Astrophys.* 569:L1. Erratum. 2015. *Astron. Astrophys.* 574:C4
- Anderson CM, Weitenbeck AJ, Code AD, et al. 1996. *Astron. J.* 112:2726
- Andersson B-G, Piirola V, De Buizer J, et al. 2013. *Ap. J.* 775:84
- Andersson B-G, Pintado O, Potter SB, Straizys V, Charcos-Llorens M. 2011. *Astron. Astrophys.* 534:A19
- Andersson B-G, Potter SB. 2005. *MNRAS* 356:1088
- Andersson B-G, Potter SB. 2007. *Ap. J.* 665:369
- Andersson B-G, Potter SB. 2010. *Ap. J.* 720:1045
- Arce HG, Goodman AA, Bastien P, Manset N, Sumner M. 1998. *Ap. J.* 499:L93
- Balbus SA. 1986. *Ap. J.* 304:787
- Battistelli ES, Rebolo R, Rubiño-Martín JA, et al. 2006. *Ap. J.* 645:141
- Bethell TJ, Chepurnov A, Lazarian A, Kim J. 2007. *Ap. J.* 663:1055
- Boogert ACA, Perakines GA, Whittet DCB. 2015. *Annu. Rev. Astron. Astrophys.* 53:541–81
- Bradley JP. 1994. *Science* 265:925
- Bradley JP. 1995. *Meteoritics* 30:491
- Bradley JP, Keller LP, Flynn GJ, Sitko ML. 2000. In *Thermal Emission Spectroscopy and Analysis of Dust, Disks, and Regoliths. ASP Conf. Ser.* 196:119. San Francisco: ASP
- Burke BF, Graham-Smith F. 1997. *An Introduction to Radio Astronomy*. New York: Cambridge Univ. Press
- Carrasco-González C, Rodríguez LF, Anglada G, et al. 2010. *Science* 330:1209
- Carrasco-González C, Rodríguez LF, Osorio M, et al. 2011. *Rev. Mex. Astron. Astrofis. Conf. Ser.* 40:229–30
- Casali MM. 1995. *MNRAS* 277:1385
- Cashman LR, Clemens DP. 2014. *Ap. J.* 793:126
- Chandrasekhar S, Fermi E. 1953. *Ap. J.* 118:113
- Chiar JE, Adamson AJ, Whittet DCB, et al. 2006. *Ap. J.* 651:268
- Chiar JE, Tielens AGGM, Adamson AJ, Ricca A. 2013. *Ap. J.* 770:78
- Cho J, Lazarian A. 2005. *Ap. J.* 631:361
- Cho J, Lazarian A. 2007. *Ap. J.* 669:1085
- Chrysostomou A, Hough JH, Whittet DCB, et al. 1996. *Ap. J.* 465:L61
- Clayton GC, Anderson CM, Magalhaes AM, et al. 1992. *Ap. J.* 385:L53
- Clayton GC, Wolff MJ, Allen RG, Lupie OL. 1995. *Ap. J.* 445:947
- Clayton GC, Wolff MJ, Sofia UJ, Gordon KD, Misselt KA. 2003. *Ap. J.* 588:871
- Clemens DP, Pinnick AF, Pavel MD, Taylor BW. 2012. *Astron. J. Suppl.* 200:19
- Clemens DP, Sarcia D, Grabau A, et al. 2007. *Publ. Astron. Soc. Pac.* 119:1385
- Codina-Landaberry S, Magalhães AM. 1976. *Astron. Astrophys.* 49:407
- Compiègne M, Verstraete L, Jones A, et al. 2011. *Astron. Astrophys.* 525:103
- Cortés PC, Crutcher RM, Matthews BC. 2006. *Ap. J.* 650:246
- Crutcher RM. 2004. *Astrophys. Space Sci.* 292:225
- Crutcher RM, Hakobian N, Troland TH. 2009. *Ap. J.* 692:844
- Crutcher RM, Nutter DJ, Ward-Thompson D, Kirk JM. 2004. *Ap. J.* 600:279
- Cudlip W, Furniss I, King KJ, Jennings RE. 1982. *MNRAS* 200:1169
- Davis L Jr. 1951. *Phys. Rev.* 81:890
- Davis L Jr., Greenstein JL. 1951. *Ap. J.* 114:206

- Désert F-X, Boulanger F, Puget JL. 1990. *Astron. Astrophys.* 237:215
- Dober B, Ade PAR, Ashton P, et al. 2014. In *Millimeter, Submillimeter, and Far-Infrared Detectors and Instrumentation for Astronomy VII*, ed. WS Holland, J Zmuidzinas. *Proc. SPIE Conf. Ser.* 9153:91530H. Bellingham, WA: SPIE
- Dolginov AZ, Mytrophanov IG. 1976. *Ap. Space Sci.* 43:291
- Dotson JL, Davidson J, Dowell CD, Schleuning DA, Hildebrand RH. 2000. *Astron. J. Suppl.* 128:335
- Dotson JL, Vaillancourt JE, Kirby L, et al. 2010. *Astron. J. Suppl.* 186:406
- Dowell CD, Cook BT, Harper DA, et al. 2010. In *Ground-Based and Airborne Instrumentation for Astronomy III*, ed. IS McLean, SK Ramsay, H Takami. *Proc. SPIE Conf. Ser.* 7735:77356H. Bellingham, WA: SPIE
- Draine BT. 2003. *Annu. Rev. Astron. Astrophys.* 41:241
- Draine BT. 2011. *Physics of the Interstellar and Intergalactic Medium*. Princeton, NJ: Princeton Univ. Press
- Draine BT, Anderson N. 1985. *Ap. J.* 292:494
- Draine BT, Flatau PJ. 1994. *J. Opt. Soc. Am. A* 11:1491
- Draine BT, Fraisse AA. 2009. *Ap. J.* 696:1
- Draine BT, Hensley B. 2012. *Ap. J.* 757:103
- Draine BT, Lazarian A. 1998a. *Ap. J.* 494:L19
- Draine BT, Lazarian A. 1998b. *Ap. J.* 508:157
- Draine BT, Lazarian A. 1999. *Ap. J.* 512:740
- Draine BT, Li A. 2007. *Ap. J.* 657:810
- Draine BT, Roberge WG, Dalgarno A. 1983. *Ap. J.* 264:485
- Draine BT, Weingartner JC. 1996. *Ap. J.* 470:551
- Draine BT, Weingartner JC. 1997. *Ap. J.* 480:633
- Egan MP, Price SD, Kraemer KE, et al. 2003. *VizieR Online Data Cat.* 5114:0
- Federman SR, Glassgold AE, Kwan J. 1979. *Ap. J.* 227:466
- Field GB, Somerville WB, Dressler K. 1966. *Annu. Rev. Astron. Astrophys.* 4:207
- Fox AJ, Wakker BP, Savage BD, et al. 2005. *Ap. J.* 630:332
- France K, Andersson B-G, McCandliss SR, Feldman PD. 2005. *Ap. J.* 628:750
- Franco GAP, Alves FO, Girart JM. 2010. *Ap. J.* 723:146
- Gerakines PA, Whittet DCB, Lazarian A. 1995. *Ap. J.* 455:L171
- Gold T. 1952a. *MNRAS* 112:215
- Gold T. 1952b. *Nature* 169:322
- Goodman AA, Jones TJ, Lada EA, Myers PC. 1992. *Ap. J.* 399:108
- Goodman AA, Jones TJ, Lada EA, Myers PC. 1995. *Ap. J.* 448:748
- Goodman AA, Whittet DCB. 1995. *Ap. J.* 455:L181
- Greenberg JM. 1968. In *Nebulae and Interstellar Matter*, ed. BM Middlehurst, LH Aller, p. 221. Chicago: Univ. Chicago Press
- Hall JS. 1949. *Science* 109:166
- Hildebrand RH. 1988. *Q. J. R. Astron. Soc.* 29:327
- Hildebrand RH, Davidson JA, Dotson JL, et al. 2000. *Publ. Astron. Soc. Pac.* 112:1215
- Hildebrand RH, Dotson JL, Dowell CD, Schleuning DA, Vaillancourt JE. 1999. *Ap. J.* 516:834
- Hildebrand RH, Dragovan M. 1995. *Ap. J.* 450:663
- Hiltner WA. 1949a. *Ap. J.* 109:471
- Hiltner WA. 1949b. *Science* 109:165
- Hoang T, Lazarian A. 2008. *MNRAS* 388:117
- Hoang T, Lazarian A. 2009a. *Ap. J.* 695:1457
- Hoang T, Lazarian A. 2009b. *Ap. J.* 697:1316
- Hoang T, Lazarian A. 2012. *Adv. Astron.* 2012:id.208159
- Hoang T, Lazarian A, Martin PG. 2013. *Ap. J.* 779:152
- Hoang T, Lazarian A, Martin PG. 2014. *Ap. J.* 790:6
- Hoang T, Lazarian A, Schlickeiser R. 2012. *Ap. J.* 747:54
- Hollenbach D, Kaufman MJ, Bergin EA, Melnick GJ. 2009. *Ap. J.* 690:1497
- Houde M, Vaillancourt JE, Hildebrand RH, Chitsazzadeh S, Kirby L. 2009. *Ap. J.* 706:1504
- Hough JH, Aitken DK, Whittet DCB, Adamson AJ, Chrysostomou A. 2008. *MNRAS* 387:797

- Hough JH, Sato S, Tamura M, et al. 1988. *MNRAS* 230:107
- Huggins PJ, Gillespie AR, Sollner TCL, Phillips TG. 1977. *Astron. Astrophys.* 54:955
- Jackson JD. 1975. *Classical Electrodynamics*. New York: Wiley. 2nd ed.
- Jansen DJ, van Dishoeck EF, Black JH. 1994. *Astron. Astrophys.* 282:605
- Jansen DJ, van Dishoeck EF, Black JH, Spaans M, Sosin C. 1995. *Astron. Astrophys.* 302:223
- Jones RV, Spitzer L. 1967. *Ap. J.* 147:943
- Jones TJ. 1989. *Ap. J.* 346:728
- Jones TJ, Bagley M, Krejny M, Andersson B-G, Bastien P. 2015. *Astron. J.* 149:31
- Jones TJ, Hyland AR, Bailey J. 1984. *Ap. J.* 282:675
- Jones TJ, Klebe D, Dickey JM. 1992. *Ap. J.* 389:602
- Kato S, Mizuno N, Asayama S-I, et al. 1999. *Publ. Astron. Soc. Jpn.* 51:883
- Kim S-H, Martin PG. 1994. *Ap. J.* 431:783
- Kim S-H, Martin PG. 1995. *Ap. J.* 444:293
- Kim S-H, Martin PG, Hendry PD. 1994. *Ap. J.* 422:164
- Klare G, Neckel Th, Schnur G. 1972. *Astron. Astrophys. Suppl.* 5:239
- Kogut A, Fixsen DJ, Levin SM, et al. 2011. *Ap. J.* 734:4
- Lada CJ, Muench AA, Lada EA, Alves JF. 2004. *Astron. J.* 128:1254
- Lazarian A. 1994. *Astrophys. Space Sci.* 216:235
- Lazarian A. 1995. *Ap. J.* 451:660
- Lazarian A. 1997. *Ap. J.* 483:296
- Lazarian A. 2003. *J. Quant. Spectrosc. Radiat. Transf.* 79:881
- Lazarian A. 2007. *J. Quant. Spectrosc. Radiat. Transf.* 106:225
- Lazarian A, Andersson B-G, Hoang T. 2015. In *Polarimetry of Stars and Planetary Systems*, ed. L Kolokolova, J Hough, A-Ch Levasseur-Regourd, pp. 81–113. New York: Cambridge Univ. Press
- Lazarian A, Draine BT. 1997. *Ap. J.* 487:248
- Lazarian A, Draine BT. 1999a. *Ap. J.* 516:L37
- Lazarian A, Draine BT. 1999b. *Ap. J.* 520:L67
- Lazarian A, Draine BT. 2000. *Ap. J.* 536:L15
- Lazarian A, Efrogmsky M. 1996. *Ap. J.* 466:274
- Lazarian A, Efrogmsky M. 1999. *MNRAS* 303:673
- Lazarian A, Efrogmsky M, Ozik J. 1996. *Ap. J.* 472:240
- Lazarian A, Hoang T. 2007a. *MNRAS* 378:910
- Lazarian A, Hoang T. 2007b. *Ap. J.* 669:L77
- Lazarian A, Hoang T. 2008. *Ap. J.* 676:L25
- Lazarian A, Hoang T. 2011. In *Astronomical Polarimetry 2008: Science From Small to Large Telescopes. ASP Conf. Ser.* 449:116. San Francisco: ASP
- Lazarian A, Roberge WG. 1997a. *Ap. J.* 484:230
- Lazarian A, Roberge WG. 1997b. *MNRAS* 287:941
- Lee HM, Draine BT. 1985. *Ap. J.* 290:211
- Léger A. 1988. In *Polarized Radiation of Circumstellar Origin*, ed. GV Coyne, AFJ Moffat, S Tapia, AM Magalhaes, RE Schulte-Ladbeck, NC Wickramasinghe, p. 769. Vatican City State/Tucson: Vatican Obs./Univ. Ariz. Press
- Léger A, Puget JL. 1984. *Astron. Astrophys.* 137:L5
- Lorenz EN. 1993. *The Essence of Chaos*. Seattle: Univ. Wash. Press
- Luhman ML, Jaffe DT, Sternberg A, Herrmann F, Poglitsch A. 1997. *Ap. J.* 482:298
- Martin PG. 1974. *Ap. J.* 187:461
- Martin PG, Adamson AJ, Whittet DCB, et al. 1992. *Ap. J.* 392:691
- Martin PG, Angel JRP. 1976. *Ap. J.* 207:126
- Martin PG, Clayton GC, Wolff MJ. 1999. *Ap. J.* 510:905
- Mathis JS. 1979. *Ap. J.* 232:747
- Mathis JS. 1986. *Ap. J.* 308:281
- Mathis JS, Mezger PG, Panagia N. 1983. *Astron. Astrophys.* 128:212
- Mathis JS, Rimpl W, Nordsieck KH. 1977. *Ap. J.* 217:425



- Matsumura M, Kameura Y, Kawabata KS, et al. 2011. *Publ. Astron. Soc. Jpn.* 63:L43
- Matthews BC, McPhee CA, Fissel LM, Curran RL. 2009. *Astron. J. Suppl.* 182:143
- Morata O, Herbst E. 2008. *MNRAS* 390:1549
- Murakawa K, Tamura M, Nagata T. 2000. *Astron. J. Suppl.* 128:603
- Netzer N, Elitzur M. 1993. *Ap. J.* 410:701
- Ominato Y, Koshino M. 2012. *Phys. Rev. B* 85:165454
- Planck Collab. XX. 2011. *Astron. Astrophys.* 536:A20
- Planck Collab. XV. 2014. *Astron. Astrophys.* 565:A103
- Planck Collab. XIX. 2015. *Astron. Astrophys.* 576:A104
- Planck Collab. XXII. 2015. *Astron. Astrophys.* 576:A107
- Plaszczynski S, Montier L, Levrier F, Tristram M. 2014. *MNRAS* 439:4048
- Polehampton ET, Wyrowski F, Schilke P. 2005. *High resolution observations of clumpy structure in IC63*. Presented at Astrochemistry throughout the Universe: Recent Successes & Current Challenges, IAU Symp. 231, Monterey, CA
- Price SD, Egan MP, Carey SJ, Mizuno DR, Kuchar TA. 2001. *Astron. J.* 121:2819
- Purcell EM. 1979. *Ap. J.* 231:404
- Quinn JL. 2012. *Astron. Astrophys.* 538:A65
- Rao R, Crutcher RM, Plambeck RL, Wright MCH. 1998. *Ap. J.* 502:L75
- Richtmyer RD, Teller E. 1949. *Phys. Rev.* 75:1729
- Roberge WG. 1996. In *Polarimetry of the Interstellar Medium*, ed. WG Roberge, DCB Whittet. *ASP Conf. Ser.* 97:401. San Francisco: ASP
- Roberge WG, Hanany S, Messinger DW. 1995. *Ap. J.* 453:238
- Roberge WG, Lazarian A. 1999. *MNRAS* 305:615
- Rubiño-Martín JA, López-Caraballo CH, Génova-Santos R, Rebolo R. 2012. *Adv. Astron.* 2012:351836
- Salgado F, Berné O, Adams JD, et al. 2012. *Ap. J.* 749:L21
- Schleuning DA, Vaillancourt JE, Hildebrand RH, et al. 2000. *Ap. J.* 535:913
- Sellgren K, Rouan D, Léger A. 1988. *Astron. Astrophys.* 196:252
- Serkowski K. 1973. In *Interstellar Dust and Related Topics*, ed. JM Greenberg, HC van de Hulst. *IAU Symp.* 52:145. Dordrecht, Neth.: Kluwer
- Serkowski K, Mathewson DS, Ford VL. 1975. *Ap. J.* 196:261
- Sironi L, Draine BT. 2009. *Ap. J.* 698:1292
- Slavin JD. 1989. *Ap. J.* 346:718
- Smith CH, Wright CM, Aitken DK, Roche PF, Hough JH. 2000. *MNRAS* 312:327
- Sorrell WH. 1995. *MNRAS* 273:169
- Spitzer L, McGlynn TA. 1979. *Ap. J.* 231:417
- Spitzer L, Tukey JW. 1949. *Science* 109:461
- Stecher TP, Williams DA. 1967. *Ap. J.* 149:L29
- Steglich M, Bouwman J, Huysen F, Henning Th. 2011. *Ap. J.* 742:2
- Stein W. 1966. *Ap. J.* 144:318
- Tamura M, Nagata T, Sato S, Tanaka M. 1987. *MNRAS* 224:413
- Tang Y-W, Ho PTP, Girart JM, et al. 2009. *Ap. J.* 695:1399
- Tibbs CT, Paladini R, Compiègne M, et al. 2012. *Ap. J.* 754:94
- Tielens AGGM. 2005. *The Physics and Chemistry of the Interstellar Medium*. Cambridge, UK: Cambridge Univ. Press
- Tokunaga AT. 2000. In *Allen's Astrophysical Quantities*, ed. AN Cox, p. 143. New York: AIP
- Vaillancourt JE. 2002. *Astron. J. Suppl.* 142:53
- Vaillancourt JE. 2006. *Publ. Astron. Soc. Pac.* 118:1340
- Vaillancourt JE. 2007. In *Sky Polarisation at Far-Infrared to Radio Wavelengths: The Galactic Screen before the Cosmic Microwave Background*, ed. F Boulanger, M-A Miville-Deschênes, p. 147. *EAS Publ. Ser.* 23. Cambridge, UK: EDP Sci.
- Vaillancourt JE, Dowell CD, Hildebrand RH, et al. 2008. *Ap. J.* 679:L25
- Vaillancourt JE, Matthews BC. 2012. *Astron. J. Suppl.* 201:13



- Voshchinnikov NV, Henning T, Prokopenko MS, Das HK. 2012. *Astron. Astrophys.* 541:A52
- Weingartner JC, Draine BT. 2003. *Ap. J.* 589:289
- Weingartner JC, Jordan ME. 2008. *Ap. J.* 672:382
- Whittet DCB. 2003. *Dust in the Galactic Environment*. Bristol: Inst. Phys. 2nd ed.
- Whittet DCB, Adamson AJ, Duley WW, Geballe TR, McFadzean AD. 1989. *MNRAS* 241:707
- Whittet DCB, Gerakines PA, Hough JH, Shenoy SS. 2001. *Ap. J.* 547:872
- Whittet DCB, Goldsmith PF, Pineda JL. 2010. *Ap. J.* 720:259
- Whittet DCB, Hough JH, Lazarian A, Hoang T. 2008. *Ap. J.* 674:304
- Whittet DCB, Martin PG, Hough JH, et al. 1992. *Ap. J.* 386:562
- Whittet DCB, van Breda IG. 1978. *Astron. Astrophys.* 66:57
- Wiebe DS, Watson WD. 2001. *Ap. J.* 549:L115
- Willing BA, Lebofsky MJ, Kemp JC, Martin PG, Rieke GH. 1980. *Ap. J.* 235:905
- Willing BA, Lebofsky MJ, Rieke GH. 1982. *Astron. J.* 87:695
- Wolfire MG, Hollenbach D, McKee CF, Tielens AGGM, Bakes ELO. 1995. *Ap. J.* 443:152
- Wynn-Williams CG. 1971. *MNRAS* 151:397
- Yan H, Lazarian A. 2002. *Phys. Rev. Lett.* 89:281102
- Yan H, Lazarian A. 2003. *Ap. J.* 592:L33
- Yan H, Lazarian A. 2015. In *Magnetic Fields in Diffuse Media*, ed. A Lazarian, EM de Gouveia Dal Pino, C Melioli, p. 89. New York: Springer
- Ysard N, Abergel A, Ristorcelli I, et al. 2013. *Astron. Astrophys.* 559:A133
- Zeng L, Bennett CL, Chapman NL, et al. 2013. *Ap. J.* 773:29



# Contents

Exploring the Universe <i>Maarten Schmidt</i> .....	1
Hypervelocity Stars <i>Warren R. Brown</i> .....	15
Physical Models of Galaxy Formation in a Cosmological Framework <i>Rachel S. Somerville and Romeel Davé</i> .....	51
Powerful Outflows and Feedback from Active Galactic Nuclei <i>Andrew King and Ken Pounds</i> .....	115
Visible/Infrared Imaging Spectroscopy and Energy-Resolving Detectors <i>Frank Eisenhauer and Walfried Raab</i> .....	155
The Nine Lives of Cosmic Rays in Galaxies <i>Isabelle A. Grenier, John H. Black, and Andrew W. Strong</i> .....	199
Ideas for Citizen Science in Astronomy <i>Philip J. Marshall, Chris J. Lintott, and Leigh N. Fletcher</i> .....	247
On the Cool Side: Modeling the Atmospheres of Brown Dwarfs and Giant Planets <i>M.S. Marley and T.D. Robinson</i> .....	279
Grid-Based Hydrodynamics in Astrophysical Fluid Flows <i>Romain Teyssier</i> .....	325
Revisiting the Unified Model of Active Galactic Nuclei <i>Hagai Netzer</i> .....	365
The Occurrence and Architecture of Exoplanetary Systems <i>Joshua N. Winn and Daniel C. Fabrycky</i> .....	409

Faltering Steps Into the Galaxy: The Boundary Regions of the Heliosphere <i>G.P. Zank</i> .....	449
Interstellar Dust Grain Alignment <i>B-G Andersson, A. Lazarian, and John E. Vaillancourt</i> .....	501
Observations of the Icy Universe <i>A.C. Adwin Boogert, Perry A. Gerakines, and Douglas C.B. Whittet</i> .....	541
Molecular Clouds in the Milky Way <i>Mark Heyer and T.M. Dame</i> .....	583
Near-Field Cosmology with Extremely Metal-Poor Stars <i>Anna Frebel and John E. Norris</i> .....	631

## Indexes

Cumulative Index of Contributing Authors, Volumes 42–53 .....	689
Cumulative Index of Article Titles, Volumes 42–53 .....	692

## Errata

An online log of corrections to *Annual Review of Astronomy and Astrophysics* articles  
may be found at <http://www.annualreviews.org/errata/astro>